How moisture shapes low-level radiative cooling in subsidence regimes

B. Fildier[1]*, C. Muller[1,2], R. Pincus[3], and S. Fueglistaler[4]

[1]Laboratoire de Météorologie Dynamique (LMD)/Institut Pierre Simon Laplace (IPSL), École Normale Supérieure, Paris Sciences & Lettres (PSL) Research University, Sorbonne Université, École Polytechnique, CNRS, F-75005 Paris, France
[2]Institute for Science and Technology, Vienna, Austria
[3]Lamont-Doherty Earth Observatory, Palisades, New York, USA
[4]Geosciences Department, Princeton University, Princeton, New Jersey, USA

Key Points:

- New theory is developed for the shape and magnitude of low-level longwave cooling peaks
- Low-level cooling scales with the boundary-layer-to-free-troposphere ratio in relative humidity
- Elevated intrusions of moist air in mid-levels can significantly damp low-level cooling

*24 rue Lhomond, 75005, Paris, France

Corresponding author: B. Fildier, benjamin.fildier@lmd.ens.fr

Abstract

Radiative cooling on the lowest atmospheric levels is of strong importance for modulating atmospheric circulations and organizing convection, but detailed observations and a robust theoretical understanding are lacking. Here we use unprecedented observational constraints from subsidence regimes in the tropical Atlantic to develop a theory for the shape and magnitude of low-level longwave radiative cooling in clear-sky, showing large peaks at the top of the boundary layer. A suite of novel scaling approximations is first developed from simplified spectral theory, in close agreement with the measurements. The radiative cooling peak height is set by the maximum lapse rate in water vapor path, and its magnitude is mainly controlled by the ratio of column relative humidity above and below the peak. We emphasize how elevated intrusions of moist air can reduce low-level cooling, by sporadically shading the spectral range which effectively cools to space. The efficiency of this spectral shading depends both on water content and altitude of moist intrusions; its height dependence cannot be explained by the temperature difference between the emitting and absorbing layers, but by the decrease of water vapor extinction with altitude. This analytical work can help to narrow the search for low-level cloud patterns sensitive to radiative-convective feedbacks: the most organized patterns with largest cloud fractions tend to occur in atmospheres below 10% relative humidity and feel the strongest low-level cooling. This motivates further assessment of these favorable conditions for radiative-convective feedbacks and a robust quantification of corresponding shallow cloud dynamics in current and warmer climates.

Plain Language Summary

In the absence of clouds, the atmosphere slowly cools down, by radiating infrared energy to outer space. This cooling is particularly important for cloud patterns because of its ability to drive atmospheric circulations, but the detailed vertical structure of radiative cooling in the cloud-free boundary layer remains poorly understood. Here, highly detailed in-situ observations from an unprecendented field campaign are analyzed, exhibiting radiative cooling more than 5 times larger than the climatological mean, in the form of sharp maxima between 1 and 3 km altitude. A novel framework is proposed, based on spectral theory, to provide analytical approximations for the structure of low-level radiative cooling in regimes of subsidence with high accuracy. This cooling is temporarily reduced by elevated layers of moist air, but observations indicate an overall cooling sufficiently large to modulate the structure of shallow clouds in the subtropics and possibly affect global climate.

1 The need for finer intuition on radiative cooling structures

Gaining more intuition on radiative transfer physics is of growing interest for atmospheric dynamicists, since unconstrained interactions between radiation and convection have been identified as key mechanisms for Earth's meteorology. In particular, radiative cooling occurring in the lower troposphere can feed atmospheric circulations that are responsible for the spatial organization of clouds in a process called *self-aggregation*, which may affect both deep and shallow clouds (Bretherton et al., 2005; Wing et al., 2017; C. Muller et al., 2022). When cooling occurs low in the boundary layer, around 1 or 2 kilometers, circulations result from the stronger surface winds accelerated by density anomalies (Shamekh et al., 2020). When elevated to 3-4 kilometers above the ground, localized longwave cooling may reinforce circulations in shallow convective areas by increasing stability below the inversion layer (Stevens et al., 2017). These horizontal gradients in longwave cooling are associated with faster cyclogenesis (C. J. Muller & Romps, 2018), wider and drier subsiding areas (Craig & Mack, 2013), and the maintenance of mesoscale shallow cloud structures (Bretherton & Blossey, 2017). Modes of deep and shallow organization involve mesoscale dynamics that are unresolved in climate models, but even

a small change therein can have a large impact (relative to CO_2 forcing magnitude) on the top-of-atmosphere radiative budget: changing shallow cloud fraction modulates the Earth's albedo, and changing the dry fraction area in subsiding regions can permit efficient cooling of the Earth's surface to space as local dry "radiator fins" (Pierrehumbert, 1994).

Testing the emergence of radiatively-driven aggregation implies to connect idealized model results with observations, and a promising avenue is to refine the correspondence between the moisture structure and radiative cooling in subsidence regimes. Indeed, idealized simulations point to the importance of longwave cooling being localized in the vertical, especially in dry subsiding regions at the top of the boundary layer, as a driving force for shallow circulations (C. J. Muller & Held, 2012; C. Muller & Bony, 2015). But the simulated modes of organization change with domain size and shape in small idealized cloud-resolving models (e.g. C. J. Muller & Held, 2012; Wing et al., 2017), which motivates the formulation of new observable criteria for self-aggregation (Holloway et al., 2017). Remote-sensing observations, in turn, do not resolve the detailed structure of radiative cooling in the lower troposphere sufficiently well (Stevens et al., 2017), which complicates the direct comparison with observations. Similarly in the middle troposphere, idealized simulations also point to the emergence of elevated moist layers at mid-levels and their association with aggregation of deep convective clouds (Stevens et al., 2017; Sokol & Hartmann, 2022), but these moist layers are also often undetected by satellite retrieval algorithms (Lerner et al., 2002; Prange et al., 2021, 2022). Thus, the present work aims at exploring the relationship between the vertical structure of humidity and low-level radiative cooling in subsiding regimes, as a means to provide simple necessary conditions for self-aggregation in the observable atmosphere, with a special focus on shallow cloud patterns.

This goal is now achievable, thanks to the unprecendented in-situ measurements of the EUREC^{4}A field campaign (Stevens et al., 2021; Albright et al., 2021), which let us explore connections between atmospheric structure, radiative cooling profiles and modes of shallow clouds organization. 2,504 soundings profiles of temperature, pressure and humidity have been retrieved in the oceanic conditions upwind of Barbados in January and February 2020 (George et al., 2021), offerring far more detailed vertical structure than is available from satellite retrievals (e.g. Stevens et al., 2017). The western Atlantic hosts a variety of shallow cloud patterns, recently labeled as Fish, Flowers, Gravel and Sugar, a visual classification that has also proved effective at distinguishing their thermodynamic structures and degree of organization (Bony et al., 2020). Fish are large elongated structures surrounded by wide dry areas; Flowers, patches of 50-80km wide regularly spaced; Gravel, often composed of cold pool rings; and Sugar, smaller fair-weather cumuli (Schulz et al., 2021; Schulz, 2022). Fish and Flower can reach the largest cloud fractions and are most effective at reflecting sunlight (Bony et al., 2020). Their relationship to radiatively-driven aggregation is however unclear: radiative processes are argued to help the maintenance of the Flower structure (Bretherton & Blossey, 2017; Narenpitak et al., 2021), but these few idealized simulations have not been yet contextualized in observations. The EUREC^{4}A dataset, further described in section 2, exhibit sharp radiative cooling peaks in the lower atmosphere, of comparable magnitude as those found in numerical simulations of radiative-aggregation.

The present work aims towards developing a robust theoretical understanding of the environmental controls that allow these strong radiative cooling rates to emerge on low levels. Profiles of radiative fluxes depend nonlinearly on the vertical distribution of multiple atmospheric species, and involve radiative effects of these species across a range of spectral frequencies, so the detailed structure of radiative cooling is often calculated with complex radiative transfer models. For most problems, smooth thermodynamic profiles are computed on global climate scales, while 'grey' solutions to radiative transfer offer simpler intuition for the magnitude and change of atmospheric radiative cooling.

The main ingredients are the height of emission to space, approximated by the level where optical depth is close to unity $\tau \approx 1$; and the cooling-to-space approximation (CTS) explains how the maximum cooling is distributed in height and spectral space (Jeevanjee & Fueglistaler, 2020a, 2020b, hereafter JF20b). However, regional variations in radiative cooling are not clearly constrained, and regimes of shallow convection exhibit profiles of temperature and humidity with richer structures than in the global average, with a dry free-troposphere overlaying a moist boundary layer. Stevens et al. (2017) note the role of moisture in affecting radiative cooling in the lowest first kilometers: a constant relative humidity is qualitatively associated with roughly uniform radiative cooling, and the presence of strong vertical moisture gradients concentrates the cooling at the top of the moist layer in the form of sharper cooling peaks. This article aims at making this observation quantitative in different regimes of cloud organization.

For this purpose, we develop new theoretical criteria for the shape and behavior of low-level radiative cooling in subsidence regimes of shallow organization, and validate the theory with EUREC^{4}A observations. We address several interlocking questions:

- What aspects of the atmospheric structure and composition control the altitude and magnitude of longwave radiative cooling peaks, in regimes of subsidence?
- How does the complex vertical structure of humidity (e.g. elevated layers of moist air) complicate this picture?
- What can this theory help to identify modes of shallow cloud organization sensitive to radiatively-driven aggregation?

The key relationships of interest are those responsible for setting the shape, amplitude and altitude of clear-sky radiative cooling peaks occurring at the top of the atmospheric boundary layer. The analysis is restrained to clear-sky longwave cooling, in order to build a clear theoretical background onto which other components may be added. Longwave radiative cooling in clear air is sufficient to drive self-aggregation (C. J. Muller & Held, 2012); shortwave heating can compensate the cooling during daytime, resulting in a net reduction in daily-mean cooling by about 30-40% (Supplementary Figure S1), but this compensation is not expected to prevent aggregation (Ruppert & Hohenegger, 2018). Cloud radiative effects, not provided by EUREC^{4}A soundings (Albright et al., 2021), would enhance aggregation by suppressing longwave cooling below cloud tops, which reinforces the contrast between dry and moist regions and the corresponding circulation (Bretherton et al., 2005; C. Muller & Bony, 2015).

We start by giving an example of cloud scenes and radiative profiles from the EUREC^{4}A field campaign in section 2. Theoretical approximations for the height, shape and magnitude of longwave low-level radiative cooling are then developed in section 3. The effect of elevated moist intrusions on the lower cooling is examined in section 4 and implications of this theory for narrowing the search for radiative-aggregation in low-level cloud patterns will be discussed in section 5, before concluding (section 6).

2 Observed shapes of longwave cooling in the tropical Atlantic

The horizontal and vertical structure of atmospheric radiative cooling is closely tied to local profiles of temperature and water vapor, as well as the spectral properties of water vapor. In this paper we investigate these links using an unprecedented set of observations: 2,504 soundings (profiles of temperature, pressure and humidity) obtained in the oceanic conditions upwind of Barbados in January and February 2020 (George et al., 2021) during the EUREC^{4}A field campaign (Stevens et al., 2021). Radiative transfer calculations are performed on sounding data to compute vertical profiles of clear-sky radiative cooling (Albright et al., 2021), as well as on idealized profiles in sections 4 and 5, with the RRTMGP-RTE correlated-K model (Pincus et al., 2019). These calculations

provide us with a dataset of "observed" and idealized radiative cooling profiles to assess the robustness of theoretical scalings in section 3 and 4.

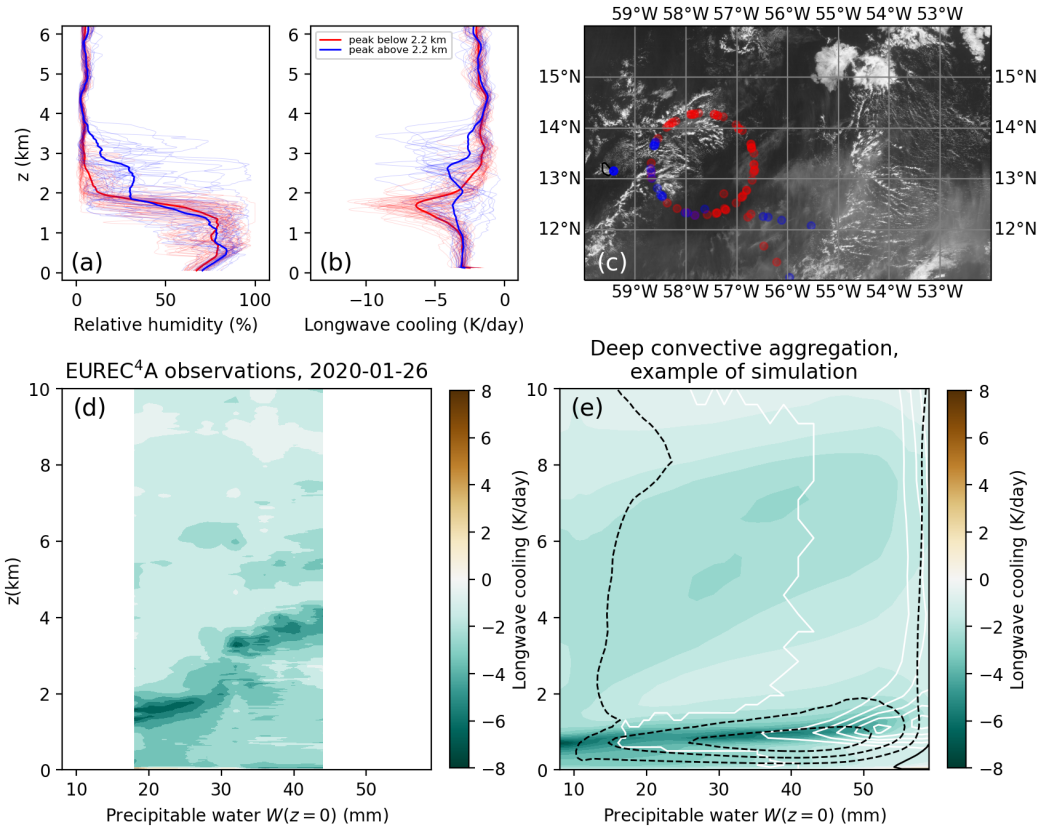

Figure 1. Observations of clear-sky longwave radiative cooling during the EUREC^{4}A field campaign, on Jan 26, 2020 (Fish pattern), showing that low-level peaks tend to occur in large and dry areas. Top row: relative humidity (a) and clear-sky longwave cooling (b) profiles (thin lines) and their means (thick lines), colored based on the height of the maximum cooling. (c) Spatial distribution of sonde positions in the cloud pattern: the image drawn is a weighted average of all GOES images retrieved from the visible channel in daytime, using isotropic Gaussian weights centered on each sonde with 10km spatial standard deviation. Lower row: clear-sky longwave radiative cooling composited as a function of column precipitable water PW from (d) Jan 26 soundings during EUREC^{4}A, and (e) in a simulation of deep convection following (C. Muller & Bony, 2015); dashed black contours are the circulation streamfunction and white contours indicate cloud water content.

An example of the rich vertical structure of humidity is given in Figure 1a for one day of the campaign (January 26, 2020) along with the corresponding profiles of longwave radiative cooling (computed by ignoring possible cloud effects (Albright et al., 2021)) in Figure 1b. These show local maxima of several K/d larger than the vertical average, coincident with sharp gradients in water vapor and temperature. Cooling peaks occur at higher altitudes in the moister convecting areas than in the drier surrounding regions (Figure 1c), possibly consistent with a surface flow from dry to moist regions (C. J. Muller & Held, 2012), efficiently diagnose in moisture space (Schulz & Stevens, 2018). Importantly, the magnitude of maximum longwave cooling observed is similar to the low-level cooling thought to promote radiative self-aggregation of deep convective clouds (Figure 1d,e).

In these limited-area simulations of deep convective aggregation, clear-sky longwave cooling is sufficient to drive convective aggregation; the subsiding environment is very dry and deep circulations are strong, implying a maximum in radiative cooling closer to the surface, while the observed cooling is maximum at higher levels. The present analysis aims at developing the analytical tools that explain the magnitude and height of radiative cooling in realistic subsiding environments, to bring context for future studies of deep *and* shallow convective aggregation.

3 Theoretical criteria for the cooling height, shape and magnitude

3.1 Main theoretical steps

We build on recent theoretical work explaining the bulk features of radiative cooling with simplified spectral theories (Jeevanjee & Fueglistaler, 2020a, 2020b). In this theory, longwave radiative cooling is dominated by cooling to space (CTS). Cooling occurs quasi-uniformly in the vertical because water vapor optical depth decreases at a fixed rate with height: at any given height, cooling occurs at wavenumbers for which optical depth is close to 1 (Jeevanjee & Fueglistaler, 2020a) and the altitude of maximum radiative cooling is controlled by the range of wavenumbers that emits the most (Jeevanjee & Fueglistaler, 2020b). Here we revisit this theory for the regional case of subsidence regimes showing a much drier free troposphere: we start with the CTS approximation and simplify the spectroscopy in a similar way as Jeevanjee and Fueglistaler (2020b), before formulating additional spectral assumptions to include the vertical structure of humidity in the theory.

3.1.1 Cooling-to-space approximation

The vertical profile of longwave radiative cooling heating rate $\mathscr{H}$ can be written as an integral over wavenumbers $\tilde{\nu}$ of the spectrally-resolved longwave heating rate $\mathscr{H}_{\tilde{\nu}}$ (in $K.s^{-1}.(\mathrm{cm}^{-1})^{-1}$):

$$\mathscr{H}(p) = \int_{\Delta\tilde{\nu}} \mathscr{H}_{\tilde{\nu}}(p) d\tilde{\nu} \tag{1}$$

where $d\tilde{\nu}$ is a unit spectral width and $\Delta\tilde{\nu}$ the spectral range of integration, defined further below in section 3.3. This heating rate $\mathscr{H}$ is typically negative so we will more generally refer to it as radiative cooling. We assume that both the background longwave radiative cooling and the local cooling maxima (negative peaks) can be modeled adequately with the cooling-to-space approximation: assuming that the photons emitted in a given layer mostly escape directly to space while exchanges between atmospheric layers are of smaller magnitude in comparison (Jeevanjee & Fueglistaler, 2020b). Under this approximation the integrand $\mathscr{H}_{\tilde{\nu}}$ is proportional to the longwave flux divergence $\partial_p F_{\tilde{\nu}}$ and can be approximated as

$$\mathscr{H}_{\tilde{\nu}}(p) = \frac{g}{c_p}\frac{dF_{\tilde{\nu}}}{dp} = \frac{g}{c_p}\pi B_{\tilde{\nu}}(T)\frac{d\mathscr{T}(\tau_{\tilde{\nu}})}{dp} \tag{2}$$

where $B_{\tilde{\nu}}$ is the Planck function, $\mathscr{T}(\tau_{\tilde{\nu}}) = e^{-\tau_{\tilde{\nu}}}$ the transmissivity at optical depth $\tau_{\tilde{\nu}}$, c_p is the specific heat capacity of air at constant pressure and g acceleration due to gravity. The vertical derivative becomes

$$\frac{d\mathscr{T}(\tau_{\tilde{\nu}})}{dp} = -\frac{d\tau_{\tilde{\nu}}}{dp}e^{-\tau_{\tilde{\nu}}} = -\frac{\beta}{p}\tau_{\tilde{\nu}}e^{-\tau_{\tilde{\nu}}} \tag{3}$$

where $\beta = \frac{d\ln\tau_{\tilde{\nu}}}{d\ln p}$ is an optical depth lapse rate, and where optical depth is defined as

$$\tau_{\tilde{\nu}} = \int_0^p \kappa_{\tilde{\nu}}(T(p'), p') q_v \frac{dp'}{g}. \tag{4}$$

where q_v is the specific humidity, approximately equal to the water vapor mixing ratio.

3.1.2 Simplified spectroscopy and optical depth lapse rate

We expand upon this framework in two ways. First, Jeevanjee and Fueglistaler (2020b) considered atmospheres with constant coefficient β, in other words, optical depth is a simple power function of pressure typical of the climatological mean. Shallow convective regimes, in contrast, are often characterized by very dry free-tropospheric conditions above the inversion level and a relatively well-mixed lower troposphere (e.g. Figure 1a). Such vertical structures in relative humidity result in strong vertical gradients in water vapor mixing ratio, so that optical depth varies can substantially deviate from a smooth climatological profile. We therefore consider the more general case of vertically varying β.

A second simplifying change is the separation of variables between the wavenumber and humidity structures. Extinction coefficients $\kappa_{\tilde{\nu}}$ have some monotonic dependence on temperature and pressure, in particular at small wavenumbers (in the rotational branch of water vapor) and large mixing ratios, but this is less pronounced in the lower troposphere below 3-4 km (Wei et al., 2019). We therefore assume $\kappa_{\tilde{\nu}}$ as constant in height in the lower troposphere and write $\tau_{\tilde{\nu}}$ as a function of water vapor path $W(p)$ above level p, $\tau_{\tilde{\nu}}(p) \approx \kappa_{\tilde{\nu}} \int_0^p q_v \frac{dp}{g} \equiv \kappa_{\tilde{\nu}} W(p)$. Furthermore, the relationship between extinction $\kappa_{\tilde{\nu}}$ and wavenumber $\tilde{\nu}$ can be approximated as a piecewise exponential function, in the rotational and the vibration-rotation band of absorption of water vapor, similarly to Jeevanjee and Fueglistaler (2020b), which makes the problem analytically tractable. Expressions are detailed in **??** and illustrated in Figure 2a for the rotational band (wavenumber range 200-1000 cm^{-1}). In practice, these expressions will allow to estimate quantitatively the radiative cooling approximations derived later, and to retrieve the two corresponding wavenumbers $\tilde{\nu}^\star$ which emit the most for a given water path W in the rotational and vibration-rotation bands, according to the relationship $\tau_{\tilde{\nu}} = \kappa(\tilde{\nu})W = 1$.

Under these assumptions, β corresponds to the lapse rate in the logarithm of water vapor path and is uniform across wavenumbers:

$$\beta \approx \frac{d \ln W}{d \ln p}. \tag{5}$$

3.1.3 Main scaling

Combining Equations 1, 2 and 3 and denoting the *weighting function* $\tau_{\tilde{\nu}} e^{-\tau_{\tilde{\nu}}}$ as $\phi_{\tilde{\nu}}$, the vertical profile of longwave cooling becomes

$$\mathscr{H}(p) \approx -\frac{g}{c_p} \frac{\beta(p)}{p} \int_{\Delta\tilde{\nu}} \pi B_{\tilde{\nu}}(T(p)) \phi_{\tilde{\nu}}(p) d\tilde{\nu} \tag{6}$$

and we denote the spectral integral by $I_{\Delta\tilde{\nu}}$ for later reference, where $\Delta\tilde{\nu}$ is the spectral range of integration determined in practice by the weighting function $\phi_{\tilde{\nu}}$. This expression can be estimated analytically and contains one main additional element compared to the one derived by Jeevanjee and Fueglistaler (2020b): the dependence of β on pressure, entirely controlled by the shape of the water vapor profile. This term will control the variations in radiative cooling amplitude across soundings. Conversely, $B_{\tilde{\nu}}$ only depends on the temperature profile, and will likely be the main degree of freedom for the increase in radiative cooling as climate warms. Lastly, $\phi_{\tilde{\nu}}$ embeds all the information about water vapor spectroscopy through extinction coefficient $\kappa(\tilde{\nu})$ and sets a constant spectral range of emission at the height of the peak (illustrated in Figure 2b).

We will now use Eq. (6) to provide a criterion for the height of radiative cooling peaks and an approximate scaling for its magnitude. A reference wavenumber $\tilde{\nu}^\star = 554\mathrm{cm}^{-1}$ will be used in the derivation, corresponding to the maximum emission at 800 hPa for an atmosphere with 10% relative humidity (see Appendix A). Superscript * is used for the emission maximum, both in the vertical dimension and spectral space ($p^\star$ denotes the pressure level of maximum spectrally-integrated emission).

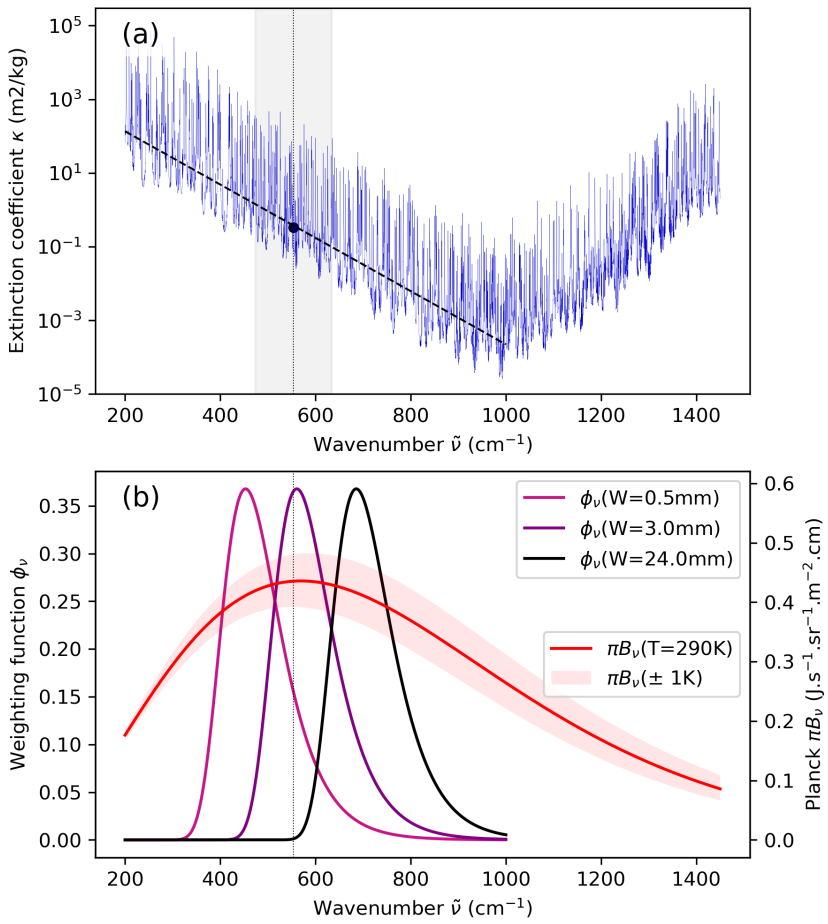

Figure 2. Spectral simplifications and emission range: (a) Water vapor extinction coefficients at reference conditions $T_{\text{ref}} = 290\text{K}$ and $p_{\text{ref}} = 800\text{hPa}$ according to the CKDMIP absorption spectra dataset (Hogan & Matricardi, 2020) (blue), the exponential fit computed following (Jeevanjee & Fueglistaler, 2020b) (black line, Appendix A). The most-emitting wavenumber $\tilde{\nu}^\star = 553\ \text{cm}^{-1}$ is computed as $\tau^\star \equiv \kappa(\tilde{\nu}^\star)W = 1$ for a typical water path $W = 3\text{mm}$ (black dot). (b) Planck function $B_{\tilde{\nu}}$ (red) and weighting functions $\phi_{\tilde{\nu}} = \kappa(\tilde{\nu})We^{-\kappa(\tilde{\nu})W}$, using the simplified analytical fit computed for $\kappa(\tilde{\nu})$: showing the smaller spectral widths of weighting functions $\Delta\tilde{\nu} = 160\ \text{cm}^{-1}$ (grey shading on panel a), found independent of W in this theory.

3.2 Physical controls on radiative cooling peak height

Jeevanjee and Fueglistaler (2020b) emphasize that the largest emission to space at fixed wavenumber $\tilde{\nu}$ is controlled by the weighting function $\phi_{\tilde{\nu}} = \tau_{\tilde{\nu}} e^{-\tau_{\tilde{\nu}}}$ which maximizes at $\tau_{\tilde{\nu}} = 1$: this result is true in τ coordinates and can be directly mapped onto height coordinates in the case of smooth zonally-averaged thermodynamic profiles. In regimes of shallow convection, optical depth relates to temperature and humidity in a non-trivial way: local radiative cooling maxima may also be obtained where T is locally maximum (inducing larger emission) and where vertical gradients in water vapor path W are large (inducing larger gradients in transmission). We consider three hypotheses for what controls the height of radiative cooling peaks, associated with each term in eq. (6):

H1) the weighting function $\phi_{\tilde{\nu}} = \tau_{\tilde{\nu}} e^{-\tau_{\tilde{\nu}}}$ peaking at $\tau_{\tilde{\nu}} = 1$,

H2) the Planck function $B_{\tilde{\nu}}(T(p))$, showing a local maximum at the inversion level where T has larger values,

H3) the optical depth lapse rate β, or W-lapse rate, corresponding to the vertical humidity structure.

These three hypotheses can be first compared graphically. Figure 3 shows a decomposition of terms appearing in equation (6) for EUREC^{4}A profiles retrieved on Jan 26, 2020. Thermodynamic profiles involved in the humidity structure are shown on the first row (panels a-c): the temperature inversion is visible in the saturation humidity profile $q_v^{sat}(T)$, and large vertical gradients in relative humidity φ and water vapor path $W(p) = \int_0^p \varphi q_v^{sat} \frac{dp}{g}$ occur below 800 hPa for the driest columns W <30 mm. This results in a sharp peak of the "humidity" parameter β, with a similar shape as the full estimate from equation (6) and as the measured cooling profile (panels h-i), which gives credit to hypothesis H3. At reference wavenumber $\tilde{\nu}^\star = 554$ cm^{-1}, the Planck term $B_{\tilde{\nu}}$ shows a small departure at the temperature inversion (panel d), and the weighting function $\phi_{\tilde{\nu}}$ shows a maximum more spread in the vertical than the target (panel e), while their joint spectral integral is smoothed in the vertical (panel f). This gives credit to the role of humidity parameter β (H3) over the Planck term or the weighting function (H1 and H2) in setting the height of the radiative cooling peak. This is finally confirmed by Figure 4b, showing all EUREC^{4}A soundings with a radiative cooling peak larger than 5 K/day below 300hPa. A clear correlation is found between the height of the hydrolapse (maximum in β) and the observed radiative peak heights. We note that a few points on Figure 4b show β peaks in the upper troposphere, while the measured cooling peak maximum occurs at lower levels. These occur in places with small-scale variability in the moisture field at upper levels, yielding large β values, but radiative cooling remains smaller due to the weaker Planck term in the upper atmosphere. These cases often correspond to upper moisture intrusions, to which we return to further below.

Analytical calculations are then made for a quantitative comparison of the role of the temperature inversion (through q_v^{sat}) and the gradient in humidity (through φ) in setting the peak of β (developed in Appendix B). We use analytical approximations for the peak amplitude, derived later in section 3.4: the drop in relative humidity at the top of the boundary layer (called *hydrolapse*) induces a cooling peak 1 or 2 orders of magnitude larger than the peak induced by the temperature inversion.

In conclusion, the height and shape of radiative cooling peaks are entirely determined by the vertical structure of relative humidity through parameter β. Besides, unlike Jeevanjee and Fueglistaler (2020b), the weighting function $\phi_{\tilde{\nu}}$ does not determine the height of maximum emission, but selects the most-emitting wavenumber $\tilde{\nu}^\star$ obeying $\tau_{\tilde{\nu}^\star} = \kappa(\tilde{\nu}^\star) W(p^\star) = 1$ at the height of radiative cooling peak (Figure 2, and Fig. 2 in (Jeevanjee & Fueglistaler, 2020b)).

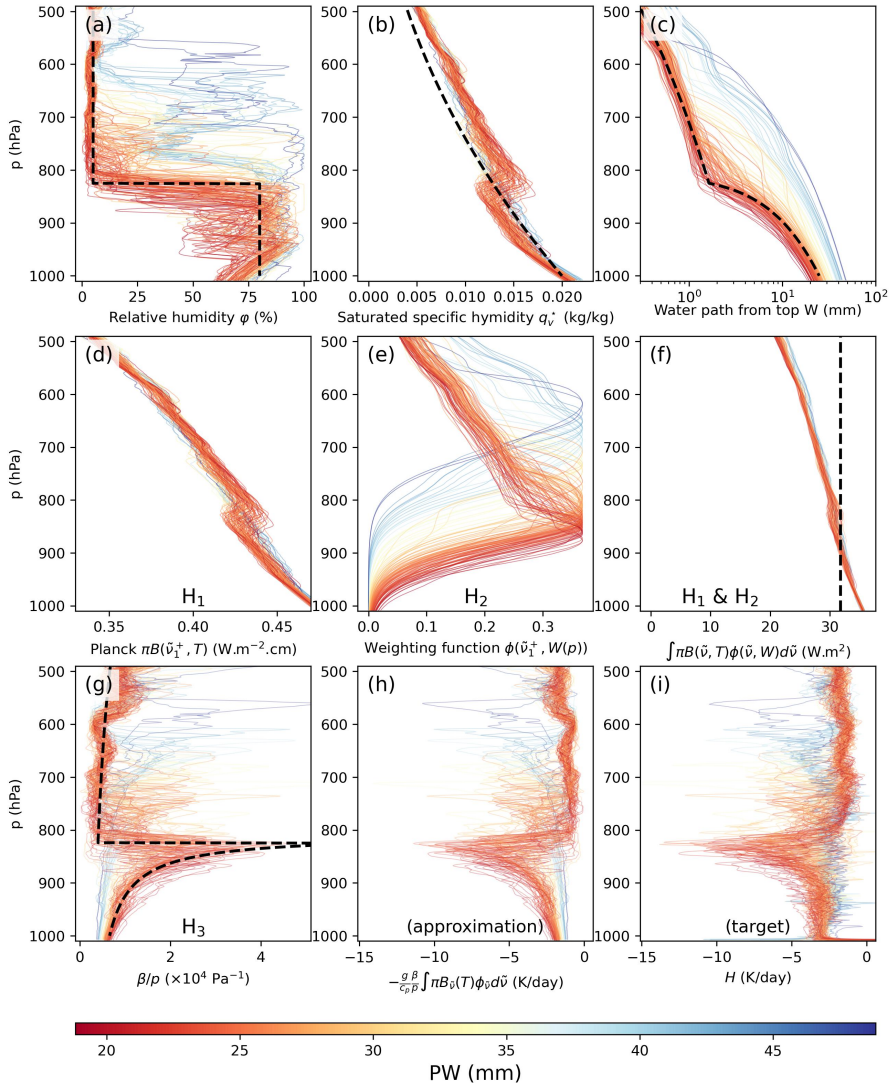

Figure 3. Decomposition of terms involved in the derivation of equation (6), illustrated with EUREC^{4}A soundings from January 26, 2020. Colors show column precipitable water and the black lines show the analytical theory derived in section 3.3, using $p^\star = 815$hPa, $\varphi_s = 80\%$, $\varphi_t = 5\%$, and $\alpha = 2.3$. The top row shows the humidity structure: Relative humidity φ approximated as a stepfunction (a), saturation specific humidity q_v^{sat} approximated as a power function of pressure ($q_v^{sat} \propto p^\alpha$) (b) and resulting water vapor path W (c), showing an inversion and a flattening of the humidity profile around 800 hPa for the driest columns. The middle row shows spectral terms: Planck emission $\pi B_{\tilde{\nu}}$ (d) and weighting functions ϕ (e) at reference wavenumber $\tilde{\nu} = 554$ cm^{-1} (corresponding to the maximum emission at 800 hPa for a water path of $W = 3$ mm at this level); these peaks are smoothed out after spectral integration $\int \pi B_{\tilde{\nu}}\phi_{\tilde{\nu}}d\tilde{\nu}$ (f). The bottom row shows the humidity parameter β/p (g) and the complete approximation to the longwave cooling profile (h) which closely match the reference longwave radiative cooling profile from RTE-RRTMGP (i).

3.3 Theory for the shape of radiative cooling profiles

Having identified the vertical structure of water vapor path (and more specifically relative humidity) as the main control for peak longwave cooling in the atmospheric boundary layer, the shape of radiative cooling can be derived analytically, from idealized thermodynamic profiles.

We first provide a simplification to the spectral integral $I_{\Delta\tilde{\nu}}$, in (6). First note that for all water paths W, the weighting functions $\phi_{\tilde{\nu}} = \kappa(\tilde{\nu})We^{-\kappa(\tilde{\nu})W}$ have the same spectral width $\Delta\tilde{\nu}$, much narrower than the Planck function (Figure 2b). Using the analytical approximation for $\kappa(\tilde{\nu})$ in Appendix A and integrating $\phi_{\tilde{\nu}}$ in spectral space gives $\int \phi_{\tilde{\nu}} d\tilde{\nu} = l_{rot} = 59$ cm^{-1}. We express it as a function of spectral width $\Delta\tilde{\nu}$, which we define as $\Delta\tilde{\nu} = \int \phi_{\tilde{\nu}} d\tilde{\nu} / \max_{\tilde{\nu}}(\phi) = l_{rot} \times e = 160$ cm^{-1}. Then, this allows to express the spectral integral $I_{\Delta\tilde{\nu}}$ as the product of $\Delta\tilde{\nu}$ and a typical Planck term $\tilde{B}$:

$$I_{\Delta\tilde{\nu}} \approx \pi\tilde{B}\frac{\Delta\tilde{\nu}}{e} \tag{7}$$

where the Planck term $\pi\tilde{B} = \pi\left(B_{\tilde{\nu}^\star_{rot}} + B_{\tilde{\nu}^\star_{vr}}\right)$ is a sum of Planck terms at reference temperature $T = 290K$ and at reference wavenumbers $\tilde{\nu}^\star_{rot}$ and $\tilde{\nu}^\star_{v-r}$, for which longwave emission is maximal in the rotational and vibration-rotation bands of water vapor. Reference $\tilde{\nu}^\star$ are detailed in Appendix A. This gives $\pi\tilde{B} = 0.56$ J.s^{-1}.m^{-2}.(cm^{-1})$^{-1}$. The Planck value only fluctuates by $\pm 4\%$ in the soundings analyzed (see $\pi\tilde{B}(\tilde{\nu}^\star_1, T)$ on Fig. 3d).

Second, we estimate β analytically from an idealized relative humidity profile (Figure 3a): a step function with value φ_s below peak level $p^\star$ and φ_t in the dry free troposphere above:

$$\varphi(p) = \varphi_t(1 - \mathbf{1}^\star(p)) + \varphi_s\mathbf{1}^\star(p) \tag{8}$$

where $\mathbf{1}^\star(p) \equiv \mathbf{1}(p - p^\star)$ is a Heaviside function equal to 1 below the peak level and 0 above. We write the saturated specific humidity profile as a power-law in pressure ($q_v^{sat} \propto p^\alpha$) (Figure 3b), where exponent α can be estimated analytically following (Romps, 2014), by approximating p and $p_v^\star$ as exponential functions of z:

$$\left\{\begin{array}{c} p_v^\star(T) \sim e^{-\frac{L_v\Gamma(z-z_0)}{R_v T^2}} \\ p \sim e^{-\frac{g(z-z_0)}{R_a T}} \end{array}\right. \quad \Rightarrow \quad q_v^{sat} = \frac{p_v^\star}{p} \sim p^\alpha \quad \Rightarrow \quad \alpha = \frac{L_v\Gamma}{gT}\frac{R_a}{R_v} - 1. \tag{9}$$

For a reference temperature of 290K, this gives $\alpha = 1.6$ in the free troposphere and $\alpha = 2.3$ in the boundary layer. Figure 3b shows the analytical profile for $\alpha = 2.3$. Then, integrating specific humidity $q_v = \varphi\, q_v^{sat}$ between 0 and p gives the corresponding idealized water vapor path W:

$$W(p) = \left\{\begin{array}{ll} W^\star\left(\frac{p}{p^\star}\right)^{1+\alpha}, & \text{for } 0 < p < p^\star \\ W^\star\frac{\varphi_s}{\varphi_t}\left(\left(\frac{p}{p^\star}\right)^{1+\alpha} - \frac{\Delta\varphi}{\varphi_s}\right), & \text{for } p^\star \leq p < p_s \end{array}\right. \tag{10}$$

where $\Delta\varphi = \varphi_s - \varphi_t$ and the water path at the jump is $W^\star = \frac{1}{\alpha+1}\frac{p_s q_{v,s}^\star \varphi_t}{g}\left(\frac{p^\star}{p_s}\right)^{1+\alpha}$. The profile of the humidity parameter $\beta(p) \equiv \frac{d\ln W}{d\ln p}$ then shows a peak of the following shape:

$$\beta(p) = (1+\alpha) \Bigg/ \left(1 - \frac{\Delta\varphi}{\varphi_s}\left(\frac{p^\star}{p}\right)^{\alpha+1}\right)^{\mathbf{1}^\star(p)} \tag{11}$$

Combining (7) and (11) into (6) yields the following expression for the radiative cooling profile:

$$\mathscr{H}(p) \approx \underbrace{-\frac{g}{c_p}\frac{1+\alpha}{p}\pi\tilde{B}\frac{\Delta\tilde{\nu}}{e}}_{\substack{\text{Constant cooling}\\ \text{in the free-troposphere}}} \Bigg/ \underbrace{\left(1-\frac{\Delta\varphi}{\varphi_s}\left(\frac{p^\star}{p}\right)^{\alpha+1}\right)^{\mathbf{1}^\star(p)}}_{\text{Cooling peak}} \tag{12}$$

Analytical profiles (8), (10), (11) and (12) are illustrated with the dashed lines on Figure 3 and 4 and show a high level of agreement with the driest soundings sampled on Jan 26. We next compare the peak height, peak magnitude and mean longwave cooling across all days of the campaign.

3.4 Scalings approximations for the amplitude of low-level cooling

To gain more intuition on the behavior of low-level cooling peaks in various large-scale environments and degrees of warming, expressions for the peak magnitude and boundary-layer-mean cooling may now be calculated. Evaluating equation (12) at peak level $p^\star$ yields the following expression for radiative cooling peak magnitude $\mathscr{H}^\star \equiv \mathscr{H}(p^\star)$:

$$\mathscr{H}^\star = -\frac{g}{c_p}\frac{1+\alpha}{p^\star}\frac{\varphi_s}{\varphi_t}\pi\tilde{B}\frac{\Delta\tilde{\nu}}{e} \tag{13}$$

and the notable result that maximum radiative cooling at the top of the boundary layer is proportional to the *ratio* between boundary-layer and free-tropospheric relative humidities. The $1/\varphi_t$ factor synthesizes the fact that a drier free-troposphere is more transparent to radiation and has larger transmittivity, and Fig. 4c shows a strong correlation and similar orders of magnitude as the EUREC^{4}A data ($r = .56$).

Also of interest for the strength of aggregation is the total amount of cooling occurring in the boundary layer. An approximation $\langle\mathscr{H}\rangle$ can be obtained by integrating equation (12) in height (detailed in Appendix C). Interestingly, the resulting expression also involves the ratio in relative humidity between the boundary layer and the free troposphere:

$$\langle\mathscr{H}\rangle = -\frac{1}{\Delta p}\frac{g}{c_p}\pi\tilde{B}\frac{\Delta\tilde{\nu}}{e}\ln\left(1+\frac{\varphi_s}{\varphi_t}\left(\left(\frac{p_s}{p^\star}\right)^{1+\alpha}-1\right)\right) \tag{14}$$

where $\Delta p = p_s - p^\star$ is the layer depth and p_s can be chosen as any level between the surface and the peak cooling height. Fig. 4d shows a strong correlation and similar orders of magnitude as the EUREC^{4}A data ($r = 0.83$).

The scalings for peak magnitude (eq. 13) and mean boundary layer cooling (eq. 14) embed the simplest formulations for thermodynamic profiles (step function in φ and power function in q_v^{sat}). Both show a proportionality to the Planck term and an increase when the free troposphere becomes drier, which remain valid in the range of humidity typically measured. Between the typical values of relative humidity observed during the EUREC^{4}A campaign (5%) to those of moist atmospheres (80%), the ratio φ_s/φ_t can vary by 1 or 2 orders of magnitude. A saturated atmosphere following a moist adiabatic temperature profile has a free tropospheric water path of 30mm above 800 hPa, so that the corresponding range in observed water path is 1.5 mm-24 mm: water vapor mostly emits between 500 cm^{-1} and 650 cm^{-1}, and the Planck term varies little (Fig. 2b). In this range, the peak cooling $\mathscr{H}^\star$ can vary by a factor 20, and the mean boundary layer cooling by a few K/day (Fig. 4b,c). The spurious divergent behavior of the $1/\varphi_t$ factor when $\varphi_t \to 0$ indicates that these expressions are not valid below the observed minimum free-tropospheric humidity of 4-5% ($W \approx 1.5$mm). Errors arise from the assumptions of heaviside function in relative humidity and of a Dirac function in spectral space for peak maximum emission, and more generally of constant spectral width of emission. At the other extreme, in the case of moist atmospheres ($\varphi_t = 80\%$, $W \approx 20$mm), the cooling peak vanishes to the climatological value of 2K/day, and the theory reduces to that of JF2020b in the absence of a hydrolapse.

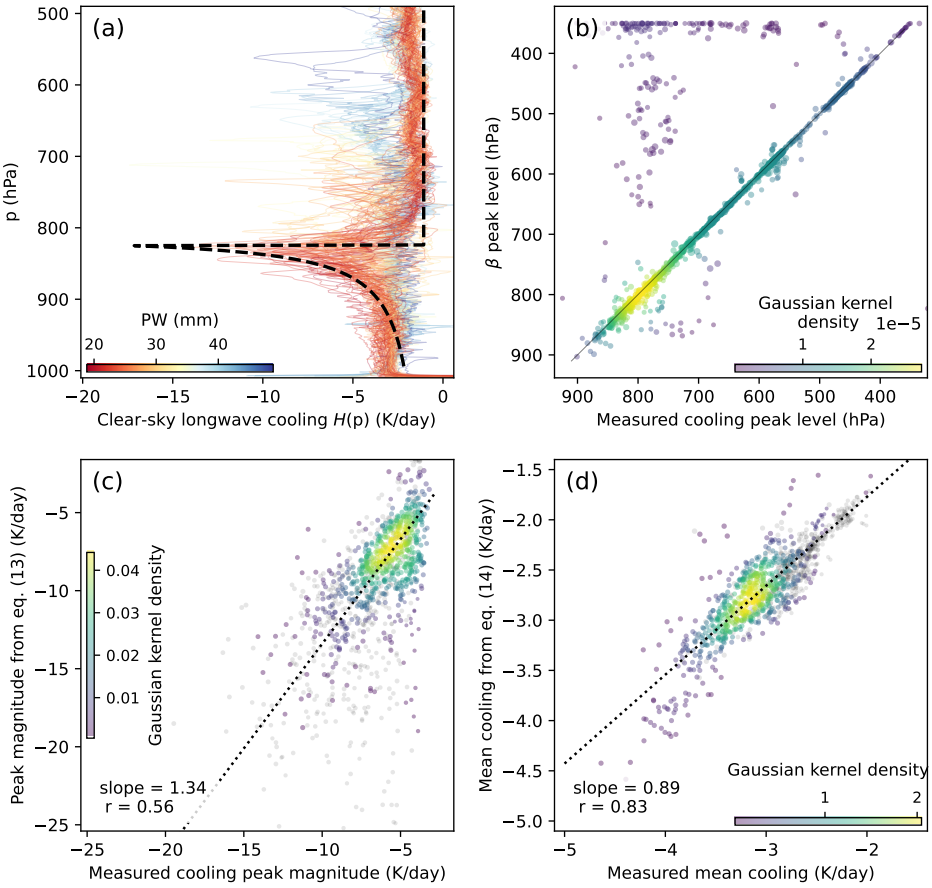

Figure 4. Correspondence between the EUREC^{4}A soundings and the analytical theory. (a) Longwave cooling profiles from Jan 26 (driest profiles in red) and example of analytical estimate using eq. (12) with φ_t =5%, φ_s =80%, α = 2.3 and our analytical fit for $\kappa(\nu)$. (b-d) correlations between *all* EUREC^{4}A soundings and the theory, for peak cooling height (b, maximum of β), peak cooling magnitude (c, eq. (13)) and integral cooling in the boundary layer (d, eq. (14)). Colors represent the density of points as fitted by a Gaussian kernel. A few points fall far from the 1:1 line on (b), when secondary peaks at the height of moist intrusions are detected instead of the main peaks (see text).

Our approximations for peak magnitude and total cooling show small biases. The cooling peak is slightly overestimated while the integral cooling is slightly underestimated. They arise from an unrealistically abrupt jump in relative humidity at the hydrolapse, resulting in a longwave cooling more concentrated at the peak height than in the underlying layers when compared with the data (Fig. 4a), and might be corrected by investigating the role of a smooth humidity transition above the boundary layer. Additional corrections may be achieved by including the effect of the temperature inversion: instead of assuming the same saturated specific humidity above and below the inversion, one can include a jump in q_v^{sat} consistent with the temperature jump ΔT (see Figure 3b). The factor φ_s/φ_t in eq (13) will be replaced by

$$\frac{\varphi_s q^\star_{v,s}(T+\Delta T)}{\varphi_t q^\star_{v,s}(T)} = \frac{\varphi_s}{\varphi_t}\exp(r_{cc}\Delta T)$$

where $r_{cc} \approx 6\%/K$ is the Clausius-Clapeyron rate of increase in q_v^{sat}. For the $\Delta T \approx$ 3K inversion observed this leads to a fractional reduction of the peak amplitude of 15-20%.

Generally, the expressions successfully highlight the factors controlling relationships between clear-sky radiative cooling and the humidity structure in the lower troposphere. They provide a framework for interpreting previous empirical results, including the observation that a moist layer overlain by a dry atmosphere radiates sharply at the interface between the two (Stevens et al., 2017). While classical theories connect radiation to metrics of optical depth or water vapor path, these equations go further and explore the link with relative humidity. This has the benefits of simplifying the physical interpretation in regimes of large-scale subsidence and of connecting radiation explicitly to convective processes. Indeed, the transition between a roughly uniform boundary layer and a dry free-troposphere is more apparent in φ-space, and the structure of relative humidity is tightly linked to mixing by convective processes in different layers of the atmosphere (Romps, 2014).

The equations above rely on three key assumptions: the CTS approximation, the separation of variables between the temperature, humidity, and spectral structures, and simplifications of spectral properties of water vapor. These assumptions are discussed in more detail in section 4, exploring cases where low-level cooling is perturbed by non-uniform free-tropospheric humidity profiles.

4 Damping of low-level cooling by elevated moist intrusions

On several days of the EUREC^{4}A field campaign, elevated layers of moist air were observed in the mid- and upper troposphere, with a damping effect on the boundary layer cooling underneath. Such intrusions may originate from congestus-level detrainment from remote deep convection, as cloudy air masses are advected into the region of analysis by southeasterly winds. Soundings that detect such intrusions are displayed on Fig.5, showing a reduction in low-level cooling peaks. Some days show a small low-level cooling peak around -4 K/day, associated with the small amount of water in moist intrusions (days 01/28 and 02/09), while others show a complete cancellation of low-level cooling peaks down to the climatological mean cooling at -2 K/day (days 02/11 and 02/13). The weaker upper intrusion on 02/13, shown in yellow, is superimposed with a lower intrusion, which explains the strong low-level damping in this case. Can the scalings derived earlier reproduce this shading effect? Which assumptions must be relaxed to explain the role of moist intrusions?

4.1 Sensitivity of low-level cooling to intrusion water content and shape

We now see that, to first order, the peak reduction follows changes in free-tropospheric humidity φ_t, or water vapor path W, which becomes more opaque as water is added above the cooling peak. This can be connected to the theory derived above, ignoring for now the small shift in emission range towards higher wavenumbers (i.e., maintaining $\tau = \kappa(\tilde{\nu}^\star)W(p^\star) = 1$) and the corresponding adjustment in the Planck term. When W increases, the hydrolapse β tends to decrease: for a fixed water vapor lapse rate dW/dp, β is inversely proportional to W. This leads to a reduction in maximum cooling in eq. (6). A larger W is directly connected to the larger free tropospheric humidity φ_t in eqs. (13-14), inversely proportional to low-level cooling. Figure 6 shows an example of strong intrusion occurring at mid-levels on Feb 13, 2020, and explores how the intrusion's shape, height and water path can modulate the reduction in low-level cooling. On panels a-b, the intrusion's shape is varied while conserving its water content: when the moist intrusion is a rectangle (in RH-space, black profile) or homogenized in the vertical (dashed black profile), the low-level peak is reduced by a similar amount as with the original triangle shape (blue profile), from 12K/day to 5K/day. Quantitatively, the scaling for peak mag-

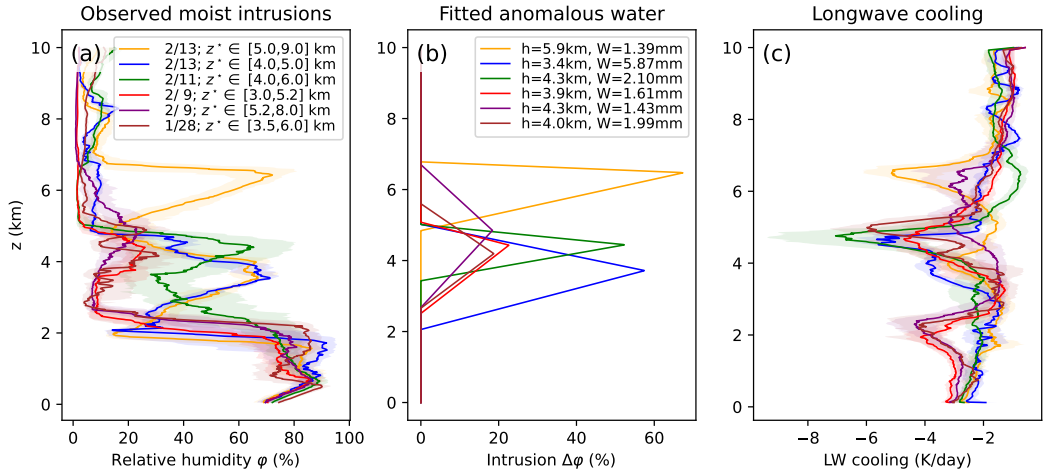

Figure 5. Elevated moist intrusions and reduction in boundary-layer longwave cooling: relative humidity grouped by day of occurrence and height of maximum longwave cooling z_p (left); anomalous relative humidity due each moist intrusion isolated from piecewise-linear fits to the median relative humidity profiles (center); corresponding clear-sky longwave cooling, showing a reduced cooling in the boundary layer and spurious peaks in the mid-troposphere above the intrusion (right). Solid lines are used for median profiles and shadings for interquartile ranges.

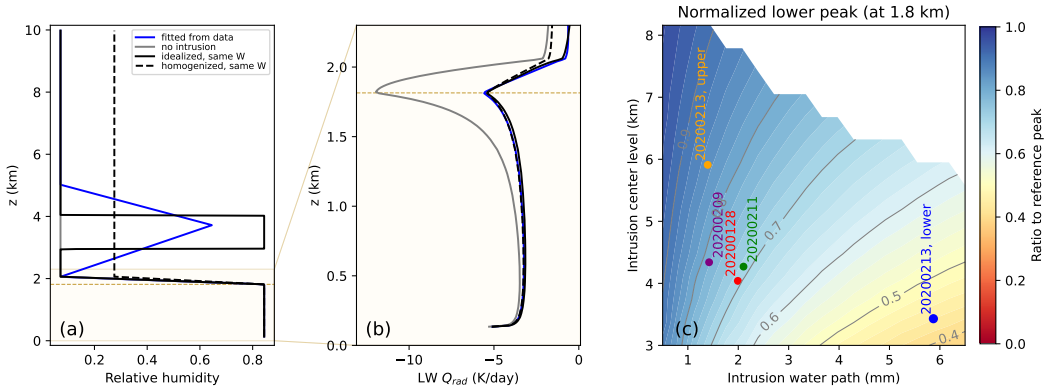

Figure 6. Reduction in low-level peak longwave cooling from elevated moist intrusions. (a) relative humidity profiles for the 2020-02-13 reference case using the lower intrusion observed fitted as a piecewise linear triangle (blue), removing the intrusion (grey) or turning it into a rectangle intrusion (solid black) or a uniform RH profile (dashed black) constructed to conserve the free-tropospheric water vapor path. (b) Zoom on the corresponding clear-sky longwave radiative cooling peak around the lower hydrolapse at 1.8 km for these four idealized cases, calculated with the RRTMGP model. (c) Reduced low-level cooling peaks normalized by the 'dry' reference (black peak divided by grey peak in panel b) as a function of the intrusion water path and center of mass (colors), calculated with the RRTMGP model. Idealized intrusions are rectangular in φ-space, and the observed moist intrusions during the EUREC^{4}A campaign are shown in this parameter space (color dots).

nitude (equation 13) overestimates the peak cooling for this strong intrusion (the ratio of free tropospheric relative humidities without and with intrusion is $\varphi_{t2}/\varphi_{t1} \approx .06/.28 \approx$

23% compared to the actual peak reduction $-5/-12 \approx 40\%$) consistently with the fact that scaling (13) overestimates the peak magnitude in the reference case (Figure 4b). But qualitatively, the reduction in cooling following a bulk increase in free-tropospheric humidity is consistent with the theory.

4.2 Sensitivity of the reduced cooling to intrusion height controlled by the vertical structure of $\kappa_{\tilde{\nu}}$

Figure 6c shows the normalized reduced peak $r = \mathscr{H}^{\star}_{int}/\mathscr{H}^{\star}_{ref}$ resulting from idealized rectangle moist intrusions at different heights and different water vapor paths. This damping in low-level cooling rates gets gradually weaker as the intrusion is higher, so that intrusion height becomes an additional degree of freedom to consider. In Figure 6b, the damping induced by the three idealized water profiles is of similar magnitude because their center of mass lies around the same altitude (≈3km). This sensitivity to height is small for small intrusions (1-2mm), with a behavior close to the theory, and is much larger for large intrusions (5-6mm). Observed intrusions during the EUREC^{4}A field campaign are shown on this parameter space: most of them occur at low water paths (around 2mm) except the one investigated in panels a-b, closer to 6mm (labeled as "20200213,lower"). In all cases, the lower the intrusion, the larger the reduction in radiative cooling underneath.

We now discuss this W/height-dependence with a few conceptual considerations and additional radiative calculations in the form of mechanism-denial experiments. Conceptually, the cooling-to-space approximation must be relaxed in the derivation above and the atmosphere may be considered as grey to get a first intuition on the height dependence. With moist intrusions, the emitted energy does not escape to space at a fixed fraction that depends on the bulk atmospheric transmissivity, but this fraction instead depends on the energy exchange between atmospheric layers. The exchange of energy between the boundary layer and the moist intrusion now depends on the difference of blackbody emission between both layers: the sensitivity of this energy exchange to intrusion height is expected to arise from the decrease in the intrusion temperature at higher altitudes, and possible changes in the layer's emissivity.

Fig. 7 provides a quantitative estimate of the normalized peaks $r = \mathscr{H}_{int}/\mathscr{H}_{ref}$ obtained with the full RRTMGP-RTE calculation, similarly as Figure 6c but when prescribing homogeneous $B_{\tilde{\nu}}$ or $\kappa_{\tilde{\nu}}$ in the vertical dimension. When both are homogenized simultaneously (Figure 7c), the low-level cooling reduction shows no dependence on intrusion height, confirming that the dependence on height is embedded in water vapor extinction coefficient or the Planck source terms. However, when the radiative calculation is reproduced by homogenizing the Planck term $B_{\tilde{\nu}}(T)$ but not the water vapor optical properties (Fig. 7a), little difference is found with the complete calculation (Fig. 6c): the Planck/temperature component is only of secondary importance. Instead, keeping water vapor extinction fixed in the vertical to its value at 800 hPa leads to substantial decrease in the reduction factor r (Fig. 6b). This result is strongly counter-intuitive, since temperature is the main height-dependent variable usually considered in "grey" radiation models of stratified atmospheres (Pierrehumbert, 2012). Neglecting the sensitivity of extinction with altitude permitted the separation of variables between $\kappa(\tilde{\nu})$ and W in section 3.3, which was a reasonable assumption for a general theory of subsidence regimes. In this section, the dependence of low-level cooling on moist intrusion height cannot be understood as a direct temperature effect, but rather through the temperature and pressure control on the vertical profile of water vapor extinction $\kappa_{\tilde{\nu}}$, and the dependence of κ with height must be accounted for when quantifying the role of moist intrusions on low-level cooling.

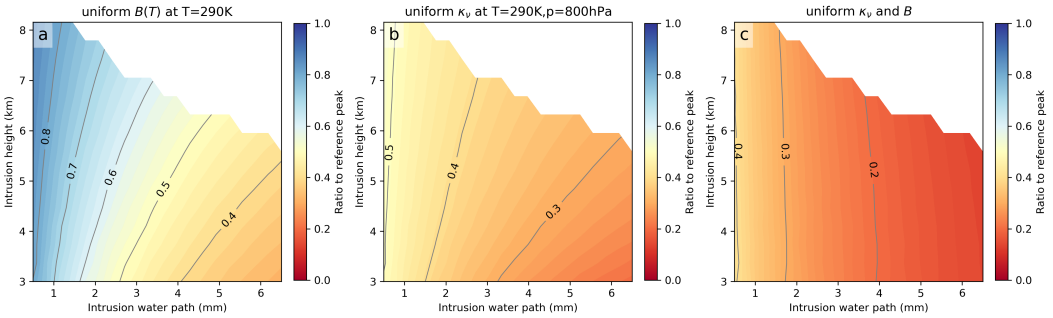

Figure 7. Mechanism denial experiments on the reduction of low-level cooling by rectangle moist intrusions of 80% relative humidity at different height and water paths, similarly to Figure 6c. The RRTMGP code is applied on the same moisture structure but now homogenizing vertically the Planck source term $B_{\tilde{\nu}}(T) = B_{\tilde{\nu}}(T^\star)$ (a), the optical properties of water vapor $\kappa_{\tilde{\nu}} = \kappa_{\tilde{\nu}}(T^\star, p^\star)$ (b), and both simultaneously (c). Overall, (a) shows a similar reduction in low-level cooling as the reference in Figure 6c and (c) shows no height dependence, similarly to the theory in section 3.4, suggesting that the sensitivity to height comes from the vertical dependence of $\kappa_{\tilde{\nu}}$.

4.3 Three mechanisms for the role of $\kappa_{\tilde{\nu}}(z)$ profiles

We then formulate three hypotheses to explain why non-uniform water vapor extinction κ can modulate the damping of low-level cooling in the presence of elevated moist intrusions. Section 4.2 supports that the intuitive approach of "grey"-radiation is ineffective, so that the answer must lie in changes in emission or absorption associated with the spectral properties of water vapor. Water vapor extinction κ decreases in height at each wavelength as a result of smaller absorber concentrations, temperatures and pressures (Wei et al., 2019). The low-level cooling can be expressed mathematically as a function of the anomalous extinction $\Delta\kappa^i = \kappa_{\tilde{\nu}}(p^i) - \kappa^\star_{\tilde{\nu}}$ occurring at intrusion level p^i. Starting from the first equality in equation 2, we note that radiative cooling is proportional to the extinction coefficient κ:

$$\mathscr{H}_{\tilde{\nu}} \propto \frac{d\tau_{\tilde{\nu}}}{dp}\frac{dF_{\tilde{\nu}}}{d\tau_{\tilde{\nu}}} \propto \kappa_{\tilde{\nu}} q_v \frac{dF_{\tilde{\nu}}}{d\tau_{\tilde{\nu}}}. \tag{15}$$

Approximating the total cooling $\mathscr{H}$ by its value at the most-emitting wavenumber $\mathscr{H}_{\tilde{\nu}^\star}$ times a fixed spectral width $\Delta\tilde{\nu}$,

$$\mathscr{H} \propto \kappa^\star \int_{\Delta\tilde{\nu}} \frac{dF_{\tilde{\nu}}}{d\tau_{\tilde{\nu}}} d\tilde{\nu} \tag{16}$$

the radiative flux divergence per unit optical depth can be decomposed in spectral space into a fraction f that directly cools to space (CTS), and a fraction $1-f$ that feels the energy exchange term between low levels and the moist intrusion (EX):

$$\left.\frac{dF_{\tilde{\nu}}}{d\tau_{\tilde{\nu}}}\right|_{int} = f \left.\frac{dF_{\tilde{\nu}}}{d\tau_{\tilde{\nu}}}\right|_{CTS} + (1-f) \left.\frac{dF_{\tilde{\nu}}}{d\tau_{\tilde{\nu}}}\right|_{EX}. \tag{17}$$

where subscript *int* denotes the presence of an intrusion and $1-f$ is the fraction of the emission range $\Delta\tilde{\nu}$ that overlaps with the spectral range of absorption within the moist intrusion. The EX term embeds the difference in Planck emission (the temperature difference) between the boundary layer and the moist intrusion: its sensitivity to intrusion height is negligible in comparison with the CTS term (consistently with section 4.2), and

for the sake of the present discussion, we can only retain the first term. Using the expression for the CTS term from section 3, we get the approximate form for low-level radiative cooling with moist intrusion:

$$\mathscr{H}_{int} \propto \kappa(\tilde{\nu}^\star_{int}) f \tilde{B} e^{-\tau^\star_{int}} \tag{18}$$

where $\tilde{\nu}^\star_{int}$ is the main emitting wavenumber at $p = p^\star$ when a moist intrusion is present and $\tau^\star_{int}$ is the free-tropospheric optical depth at $p = p^\star$ when a moist intrusion is present. Dividing by the longwave cooling in a reference atmosphere without intrusion $\mathscr{H}_{ref} \propto \kappa(\tilde{\nu}^\star_{ref}) B e^{-\tau^\star_{ref}}$ gives the following approximation for the reduction factor r:

$$r \approx \underbrace{\frac{\kappa(\tilde{\nu}^\star_{int})}{\kappa(\tilde{\nu}^\star_{ref})}}_{\substack{M1 \\ \text{emission}}} \times \underbrace{f}_{\substack{M2 \\ \text{spectral} \\ \text{overlap}}} \times \underbrace{e^{-(\tau^\star_{int} - \tau^\star_{ref})}}_{\substack{M3 \\ \text{transmission}}} \tag{19}$$

These three terms correspond to three mechanisms M1-M3 that connect the dependence of low-level cooling on intrusion height to the vertical decrease in extinction κ:

- M1) a shift in the most-emitting wavenumber $\tilde{\nu}^\star$ which enhances emission at $p = p^\star$. The smaller extinction at the height of the intrusion, reduced by an anomaly $\Delta\kappa^i = \kappa^i - \kappa^\star$, leads to a smaller optical depth $\tau(\tilde{\nu}, p^\star)$ at each wavenumber $\tilde{\nu}$, by a negative anomaly $\Delta\kappa^i \Delta W^i$. To maintain the constraint $\tau_{\tilde{\nu}^\star, p^\star} = 1$, the main emission at low levels shifts to smaller wavenumbers to enhance the extinction $\kappa(\nu^\star, p^\star)$ and the low-level emission by an amount:
$$M1 \propto \left(1 - \Delta\kappa^i \Delta W^i\right) > 1$$
- M2) a reduction in the spectral overlap $1-f$. The range of upwelling longwave radiation that is reabsorbed by the moist intrusion is smaller when κ decreases in height. This spectral shift is illustrated on Figure 8: with moist intrusions in solid blue and dotted blue containing the same water amount (panel a), the highest intrusion show a spectral range of absorption slightly shifted to the left (blue shadings centered on the blue dots, panel b). This calculation uses vertically-uniform $\kappa(\tilde{\nu})$, and when including a gradual decrease in κ with height, the absorption range shifts further to the left (red shading), reducing the overlap with the range of emission at low levels (grey shading).
- M3) an increase in the intrusion transmissivity at each wavelength. The reduced extinction at the intrusion height leads to a decrease in intrusion optical thickness by the same anomaly $\Delta\kappa^i \Delta W^i$, so that upwelling radiation at fixed $\tilde{\nu} = \tilde{\nu}^\star$ is less reabsorbed by the intrusion. This increased transmissivity within the intrusion appears as
$$M3 \propto e^{-\Delta\kappa^i \Delta W^i} > 1$$

In summary, moist intrusions can strongly reduce low-level cooling peaks by providing additional opacity above the boundary layer. Intrusion height is an important degree of freedom to consider: boundary-layer cooling peaks can be nearly cancelled by intrusions that are moist enough and close enough to the inversion. This altitude dependence likely results from the decrease in extinction coefficient with height due to pressure scaling, and from spectral effects illustrated on Fig. 8b. Three hypotheses M1-M3 are formulated for the exact mechanism through which this reduction occur, but which mechanism, if any, dominates is unknown. The general behavior is a reduced reabsorption of the upwelling radiation emitted at low levels in the spectral range of absorption at the intrusion level, for more elevated intrusions: this reduced "spectral shading" highlights the importance of diagnosing the occurrence and persistence of these layers of water vapor (Stevens et al., 2017; Prange et al., 2021), and investigating the detailed relationship with water vapor spectroscopy. Elevated moist layers, often ignored from most

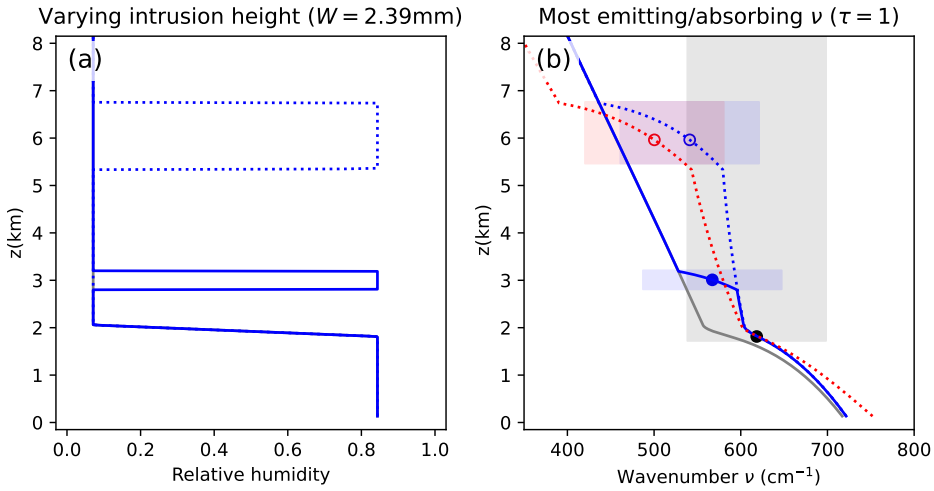

Figure 8. Reduced spectral overlap due to the vertical dependence of extinction $\kappa_{\tilde{\nu}}$. (left) relative humidity profiles for the 2020-02-13 reference case (grey) and two idealized rectangular intrusions for $W = 2.4$ mm centered at 3km and 6km; (right) the corresponding curves show the wavenumber of main emission/absorption at each height, calculated according to $\tau(z) \approx \kappa^{\star}_{\tilde{\nu}} W^{\star} + \Delta\kappa_{\tilde{\nu}} \Delta W^{i} = 1$ (equation (**??**)), using vertically uniform $\kappa_{\tilde{\nu}}$ (grey and blue curves) or a linear decrease in extinction $\partial_z \kappa_{\tilde{\nu}} = -0.1$ m^2/kg/km (red curve). Dots indicate the center of mass and main absorbing wavenumber in each case, and rectangles indicate the intrusion depth and range of absorption, assumed constant at $\Delta\tilde{\nu} = 160$ cm^{-1}; the black dot and grey shading are the main wavenumber and range of emission at the low-level peak.

idealized studies of aggregation, could play an important role in modulating convective organization in the real atmosphere (Sokol & Hartmann, 2022).

5 Implications and discussion

5.1 Possible constraints on shallow organization

We now possess a refined understanding on the relationship between low-level cooling and relative humidity, as well as the conditions in which this relationship may break: the presence of elevated moist layers. We can now focus on the background profiles observed during the EUREC^{4}A campaign, by omitting the four days when such elevated layers occur, and ask whether radiative cooling interacts with climate-relevant cloud patterns. Notably, in which cloud patterns may a self-aggregation feedback occur and be most effective?

We retain 11 days of the campaign gathering more than 100 soundings per day, and label them (Figure S2) according to a classification made on a wider spatial domain (Stevens et al., 2020; Schulz, 2022). Of special interest are Fish patterns, elongated cloud structures surrounded by wide dry areas, and Flowers, regularly-spaced circular cloud structures of 50-70km diameter. These are the most organized features observed with distinct convecting and subsiding regions, and the most interesting for climate feedbacks because of their large cloud fractions and albedo (Bony et al., 2020).

Figure 9 summarizes the connection between cloud fraction and the main predictor in our theory (equations (13) and (14)): clear-sky free-tropospheric relative humidity. The general anticorrelation suggests that patterns occurring in drier environments

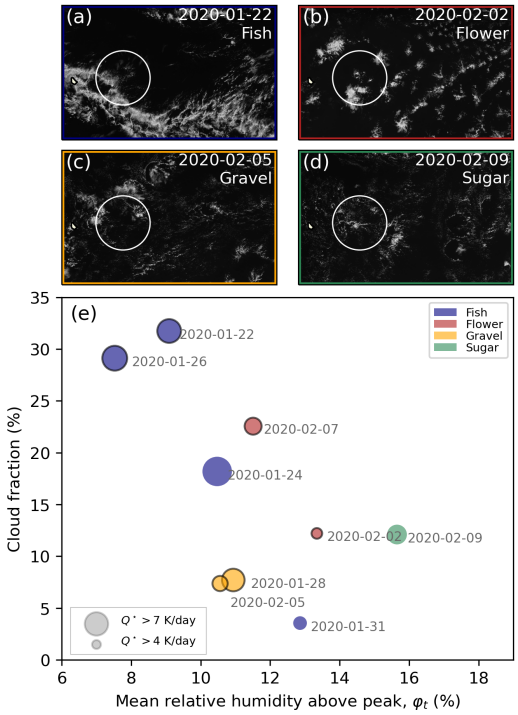

Figure 9. Relationship between shallow organization and free-tropospheric relative humidity. (a-d) example of 4 reference patterns in the classification Fish-Flower-Gravel-Sugar observed during the EUREC^{4}A campaign. (e) Daily-mean cloud fraction vs. free-tropospheric relative humidity averaged across soundings falling through clear-sky each day. Colors indicate pattern type, circled black for days with more than 20 'dry' soundings (precipitable water below 30 mm). Marker size indicate total boundary-layer cooling, from 950hPa up to the peak height. Soundings are counted as clear-sky if all levels measured are below 95% relative humidity.

are also those with the largest cloud fraction and thus the strongest effect on the global climate state. One pattern appears of greater interest, the Fish pattern: on three days (Jan 22, 24 and 26) cloud fractions are around or above 20%, free-tropospheric relative humidity below 10% and boundary layer cooling above 7K/day (with maxima of individual profiles larger than 10K/day). The other strong Fish case of Feb 13 also has a cloud fraction of 30% but relative humidity above 20% due to the mid-level moist intrusion and does not appear on this graph. Among the two organized patterns Fish and Flower, Fish shows the strongest low-level cooling, associated with drier conditions around the inversion at 4 km altitude (Figure S3). Moister conditions for Flowers may result from cloud detrainment at cloud top and the shorter distance between clouds. Other patterns are generally weakly organized with more spatially homogeneous radiative cooling, so shallow convective self-aggregation is less likely. Figure S4 also shows cooling height, peak cooling magnitude and mean boundary layer cooling as a function of column precipitable water, for all soundings and patterns. Fish patterns reach strongest clear-sky longwave cooling down to 1-2km altitude in their wide driest regions ($PW < 26$mm), which makes them best candidates for strengthened shallow circulations due to low-level clear-sky cooling.

Thus, Fish patterns, organized on the largest scales, are consistent with large radiative cooling rates in the boundary layer, so that a self-aggregation radiative feedback can be expected. Further numerical analysis is desirable to determine the importance

of this relationship between radiation and cloud organization in subsidence regimes, notably for cloud cover. Here, the inverse relationship between radiative cooling and free-tropospheric relative humidity, found in theoretical section 3.4, also allows us to provide a necessary criterion for the search of self-aggregation mechanisms in observed shallow convective regimes. Equation (13) indicates that atmospheres drier than 10-11% relative humidity have radiative cooling values stronger than -8K/day, Fig. 8 suggests that this value can be a useful threshold to narrow the search for patterns subject to self-aggregation in the current atmosphere.

5.2 Low-level cooling in a warmer world

The low-level cloud feedback remains a major source of uncertainty for global warming, and the previous section highlights a regime of convection where radiative aggregation is possible. This regime, labeled as Fish, contributes to cooling down the Earth from the two correlated factors shown on Figure 9: the large cloud fractions more effective at reflecting sunlight, and the decreased free-tropospheric humidity allowing larger outgoing longwave radiation, in the dry subtropics known as "dry radiator fins" (Pierrehumbert, 1994). Although the synoptic conditions in which these patterns emerge may or may not be favored by climate change (Schulz et al., 2021), increased shallow circulations and the degree of self-aggregation would promote maintenance of these patterns. We now discuss how the present theory can inform this discussion, by providing first insights and a clear roadmap to quantify the behavior of low-level radiative cooling in a warmer world. Equation (13) highlights three components that must be investigated to provide a robust answer: the Planck term $B_{\tilde{\nu}}(T)$, the background humidity φ_t (possibly perturbed by moist intrusions) and the spectral window of emission $\Delta\tilde{\nu}$.

A first order calculation explores the role of moist adiabatic warming in the 300-340K range of surface temperatures, using the reference relative humidity profile from Jan 26 (Fig. S5). Low-level longwave cooling is found to increase with surface warming, from -9K/day to -30K/day. In this calculation, relative humidity is fixed, so that enhancement in the cooling peak only results from the Planck response (fixed φ_s/φ_t in equations (14-13)). This response may be modulated by changing relative humidity in subsidence regions due to a slower atmospheric circulation and a changing inversion height with surface warming (Singh & O'Gorman, 2012), which can be investigated through global climate modeling and well-designed regional simulations.

Importantly, changes in the effective spectral window of emission $\Delta\tilde{\nu}$ must also be explored. Spectral effects can result from the presence of moist intrusions as discussed in section 4, but also from changes in the water vapor continuum and from overlap of this emission range with CO_2 absorption lines. The H_2O absorption continuum and CO_2 absorption range have been of strong interest from the perspective of surface emission to space, when arguing that the water vapor window closes with warming for tropical-mean thermodynamic conditions (Seeley & Jeevanjee, 2021; Kluft et al., 2021). Instead, in the case of boundary layer cooling observed in the subsidence regimes of EUREC^{4}A observations, the spectral range of emission varies weakly in the 8%-18% relative humidity profiles above the boundary layer, so that emission in the rotational band of water vapor may remain distinct from the spectral range of absorption by CO_2. Additional calculations for day Jan 26 (not shown) with and without full water-vapor continuum and CO_2 absorption in a similar spirit as Figure S5, also suggest that neither H_2O window closure not CO_2 overlap affect cooling peaks at 2km altitude even when surface temperatures rise to 340K. This can be explained by the smaller temperatures at the top of the boundary layer and the smaller optical depth in dry free-tropospheric conditions. Further analyses are necessary, with realistic estimates of futures changes in CO_2 concentrations, relative humidity and temperature profiles in subsiding regimes.

6 Conclusion

A new theory is developed to provide simplified analytical expressions for boundary layer cooling in the longwave, in the dry subtropics in clear sky. These new formulae provide a step towards building a future theory for self-aggregation, and can help to narrow the search for possible radiatively-driven circulations in the observable atmosphere. Presently, a detailed characterization of longwave radiative cooling in the shallow convective boundary layer is lacking, both theoretically and observationally. This work focuses specifically on clear-sky radiation occurring in the longwave range of the spectrum: this is the background longwave cooling onto which shortwave heating and cloud radiative effects may be added to capture the full spatial structure of radiative cooling and the partial cancellation occurring during daytime.

To this end, we focused on a region of large-scale subsidence with novel and vertically well-resolved data from the EUREC^{4}A field campaign: the measurements show longwave radiative cooling localized in the boundary layer with magnitudes comparable to simulations of convective aggregation (section 2). Analytical scalings were derived in section 3 for the height, shape and magnitude of radiative cooling peaks (eq. 6, 13, 14). They permitted to gain more robust intuition on three basic properties of the cooling profile: 1) the height and shape of low-level cooling peaks is fully determined by the moisture structure (in particular where the hydrolapse $\beta \propto \frac{dW}{dp}/W$ occurs, eq. 11); 2) the spectral structure of emission appears through a weighting function $\tau e^{-\tau}$, and selects a narrow range of emitting wavenumbers $\Delta\tilde{\nu} = 160$ cm^{-1} centered around 554 cm^{-1}, a value determined by the overlaying water vapor path; and 3) the magnitude of radiative cooling depends on the ratio of column relative humidity below and above the peak (eqs. 13-14). This connection to relative humidity will permit a more explicit connection between radiative cooling and atmospheric moistening by convective processes, the detail of which is a key unknown for atmospheric dynamicists working on radiation-convection interactions.

Strong emphasis is made on the role of elevated layers of moist air, called moist intrusions. These intrusions are occasionally transported from lower latitudes and sporadically reduce or cancel low-level cooling, but they can be missed by satellite retrieval algorithms (Prange et al., 2021, 2022) despite being major components of the large-scale circulation (Sokol & Hartmann, 2022). After detailed analysis in section 4, we conclude that intrusion mass and altitude are important degrees of freedom in the reduction of low-level cooling by moist intrusions. Interestingly, this height dependence is not explained by a temperature difference between the emitting layers and the absorbing moist intrusion, but instead by the reduction in water vapor extinction in altitude from pressure scaling and lower water vapor mixing ratios. Two mechanisms are advanced: when intrusions occur at higher altitudes, (1) the emission range slightly shifts to lower wavenumbers, leading to an increase in emission, and (2) the absorption of upwelling radiation within the intrusion is reduced and displaced in spectral space, reducing the spectral overlap. This height-dependent "spectral shading" motivates future theoretical work to capture the radiative effects of elevated moist intrusions within an effective spectral emission window $\Delta\tilde{\nu}$ to be used in eqs. 13-14. It also calls for an exploration of elevated moist layers with novel detection techniques (Prange et al., 2022), using upcoming remote sensing instruments with high vertical resolution (e.g. Krebs, 2022).

This theoretical work provides insights into the search of low-level cloud patterns subject to convective self-aggregation, and in their possible occurrence in warmer climates (section 5). Cloud patterns labeled as Fish, elongated structures of organized shallow clouds, have cloud fractions between 20% and 30%, occur in the driest wide areas effective at cooling the Earth's surface and appear consistent with radiative self-aggregation because of large values of low-level radiative cooling. A maximum value of 10-11% relative humidity in the overlaying free troposphere appears as a useful criterion to look for the occurrence of radiative self-aggregation mechanisms from remote-sensing obser-

vations. Expanding on the theoretical results obtained for future climate suggests that low-level radiative cooling may strongly increase due to Planck emission, although the free-tropospheric humidity may change with the slow down of the general circulation or the presence of moist intrusions. We also recommend further investigation of the spectral behavior of the emission window in the dry boundary layer, in conjunction with increases in the water vapor absorption continuum and saturation of the CO_2 absorption lines. Finally, this work suggests emphasis on numerical simulations of Fish patterns and their large-scale environment, the best candidates for radiative aggregation feedbacks. With rising SSTs, enhanced pattern's lifetime would promote patterns with large shallow cloud fractions and the dryness of their clear-sky surroundings. If at play, this would imply that the Earth's subtropics may reflect more sunlight in the future, and simultaneously allow the surface to cool more efficiently to space, a negative feedback on global warming.

Appendix A Spectral fit $\kappa(\tilde{\nu})$ and reference wavenumber

Under the assumption that extinction $\kappa_{\tilde{\nu}}$ only weakly varies in the range of temperature, pressure and water vapor of interest, κ can be expressed analytically as a function of wavenumber $\tilde{\nu}$ in the rotational band of water vapor, similarly to (Jeevanjee & Fueglistaler, 2020b):

$$\kappa(\tilde{\nu}) = \kappa_{rot} \exp\left(-\frac{\tilde{\nu} - \tilde{\nu}_{rot}}{l_{rot}}\right) \tag{A1}$$

Here, using reference values of $T = 290$K and $p = 800$ hPa, we find parameters $\kappa_{rot} = 131$ m^2/kg, $\tilde{\nu}_{rot} = 200$ cm^{-1} and $l_{rot} = 59.2$ cm^{-1}. The fit is performed using absorption spectra from the Correlated-K Distribution Model Intercomparison Project (CKDMIP, Hogan & Matricardi, 2020).

A similar fit can be derived for the rotation-vibration band, yielding

$$\kappa(\tilde{\nu}) = \kappa_{vr} \exp\left(\frac{\tilde{\nu} - \tilde{\nu}_{vr}}{l_{vr}}\right), \tag{A2}$$

with $\kappa_{vr} = 4.6$ m^2/kg, $\tilde{\nu}_{vr} = 1450$ cm^{-1} and $l_{vr} = 46$ cm^{-1}.

These analytical expressions can be used to calculate a reference wavenumber $\tilde{\nu}^\star$ (shown on Fig. 2), used to simplify calculations and to visualize profiles on Fig. 3-4. By choosing $\tilde{\nu}^\star$ so that $\phi_{\tilde{\nu}^\star}$ maximizes around 800 hPa ($\tau^\star = \kappa_{\tilde{\nu}^\star} W(p = 800\text{hPa}) = 1$, with $W(p = 800\text{hPa}) \approx 3$ mm for a free troposphere of 10% relative humidity), we get $\kappa^\star \equiv \kappa_{\tilde{\nu}^\star} \approx 0.3$ m^2/kg, which corresponds to $\tilde{\nu}^\star_{rot} = 554$ cm^{-1} in the rotational band of water vapor (Figure 2a), and $\tilde{\nu}^\star_{vr} = 1329$ cm^{-1} in the vibration-rotation band. In practice, the radiative cooling structure at $\tilde{\nu}^\star_{rot}$ is a good approximation for the full radiative calculation, because the Planck term is 4 to 5 times larger at $\tilde{\nu} = \tilde{\nu}^\star_{rot}$ than at $\tilde{\nu} = \tilde{\nu}^\star_{vr}$.

Appendix B Temperature and humidity contributions to cooling peak height and magnitude

The vertical temperature profile may induce a cooling peak through the Planck term and the saturation specific humidity q_v^{sat} (H2), while a jump in relative humidity may induce a peak through β (H3). These may occur on distinct atmospheric levels, and only the one resulting in the largest magnitude will be identified as the "observed" peak. To discriminate between the two, we compare the magnitude $\mathscr{H}^\star_\theta$ of a cooling peak resulting from a step function in potential temperature θ at $p = p^\star_\theta$, with the magnitude $\mathscr{H}^\star_\varphi$ of a cooling peak resulting from a step function in relative humidity φ at $p = p^\star_\varphi$. We assume that $p^\star_\theta \leq p^\star_\varphi$, although a similar reasoning can be made when $p^\star_\theta > p^\star_\varphi$.

Cooling magnitudes $\mathscr{H}_\theta^\star$ and $\mathscr{H}_\varphi^\star$ can be derived using the approximate scaling derived in equation (12), reminded here:

$$\mathscr{H}(p^\star) \approx -\frac{g}{c_p}\frac{\beta(p^\star)}{p^\star}\pi\tilde{B}\frac{\Delta\tilde{\nu}}{e} \tag{B1}$$

In this expression, vertical variations in relative humidity will only affect β, while temperature variations will affect both the Planck function $\tilde{B}$ and β (through changes in q_v^{sat}). Because these two temperature effects work in opposite directions, we can restrict our reasoning to the temperature effect on the Planck term without loss of generality. Using equation (11) above and at the peak level $p^\star$, equation (B1) becomes

$$\mathscr{H}_\theta^\star = -\frac{g}{c_p}\frac{1+\alpha}{p_\theta^\star}\pi\tilde{B}(T+\Delta T)\frac{\Delta\tilde{\nu}}{e} \tag{B2a}$$

$$\mathscr{H}_\varphi^\star = -\frac{g}{c_p}\frac{1+\alpha}{p_\varphi^\star}\frac{\varphi_s}{\varphi_t}\pi\tilde{B}(T)\frac{\Delta\tilde{\nu}}{e} \tag{B2b}$$

and we choose the same reference temperature T in both Planck functions for simplicity.

We now show that the peak cannot be controlled by the temperature structure, given the strong amplitude of the hydrolapse, by comparing $\mathscr{H}_\theta^\star$ and $\mathscr{H}_\varphi^\star$:

$$\frac{\mathscr{H}_\theta^\star}{\mathscr{H}_\varphi^\star} = \left(1+\frac{\Delta T}{\tilde{B}}\frac{\partial\tilde{B}}{\partial T}\right)\frac{\varphi_t}{\varphi_s}\frac{p_\varphi^\star}{p_\theta^\star} = \left(1+\frac{hc\tilde{\nu}/k_BT}{1-e^{-hc\tilde{\nu}/k_BT}}\frac{\Delta T}{T}\right)\frac{\varphi_t}{\varphi_s}\frac{p_\varphi^\star}{p_\theta^\star} \tag{B3}$$

where $h = 6.626\times10^{-34}$ m^2.kg.s^{-1} is the Planck constant, $c = 2.99\times10^8$ m/s is the speed of light, $k_B = 1.38\times10^{-23}$ m^2.kg.s^{-2}.K^{-1} is Boltzmann's constant, $\tilde{\nu} = \tilde{\nu}_1^\star = 554$ cm^{-1} is the reference wavenumber (we limit the reasoning to the rotational band of water vapor alone, for simplicity) and $T = 290$K the reference temperature. This gives $hc\tilde{\nu}/k_BT = 2.75$, and $hc\tilde{\nu}/k_BT/(1-e^{-hc\tilde{\nu}/k_BT}) = 2.94$. For a temperature inversion of a few degrees, $\Delta T/T \sim \mathcal{O}(10^{-2})$, and the humidity drop observed is $\varphi_t/\varphi_s \sim 0.1$. Assuming that both peak heights are between 900hPa and 500hPa, we restrict $\frac{p_\varphi^\star}{p_\theta^\star} < 2$. This gives $\mathscr{H}_\theta^\star/\mathscr{H}_\varphi^\star \ll 1$ and proves that longwave radiative cooling peak height is set by the vertical structure of humidity.

Appendix C Mean boundary layer cooling

The average cooling occurring in the boundary layer can be calculated from equation (12) approximating the full profile of low-level cooling, by integration between the level of maximum cooling (the level of the hydrolapse $p^\star$) and a pressure level close to the surface, p_s. Here we take $p_s = 950$hPa slightly above the surface, because the first layers are affected by radiative exchanges with the ocean surface, a term ignored here. We use a simple change of variable $\eta = \left(\frac{p^\star}{p}\right)^{1+\alpha}$ to integrate β/p (equation (11) divided by p) between $p^\star$ (i.e. $\eta^\star = 1$) and p_s:

$$I(p^\star, p_s) = \int \frac{d\eta}{\eta\left(1 - \frac{\Delta\varphi}{\varphi_s}\eta\right)} \tag{C1}$$

$$= \int \frac{d\eta}{\eta} + \int \frac{d\eta}{1 - \frac{\Delta\varphi}{\varphi_s}\eta} \frac{\Delta\varphi}{\varphi_s} \tag{C2}$$

$$= \ln\left(\frac{\eta_s}{\eta^\star}\right) + \ln\left(\frac{1 - \frac{\Delta\varphi}{\varphi_s}\eta^\star}{1 - \frac{\Delta\varphi}{\varphi_s}\eta_s}\right) \tag{C3}$$

$$= \ln\left(\frac{1 - \frac{\Delta\varphi}{\varphi_s}}{\frac{1}{\eta_s} - \frac{\Delta\varphi}{\varphi_s}}\right) \tag{C4}$$

$$= -\ln\left(\frac{\varphi_s}{\varphi_t}\left(\frac{p_s}{p^\star}\right)^{1+\alpha} - \frac{\Delta\varphi}{\varphi_t}\right) \tag{C5}$$

$$= -\ln\left(1 + \frac{\varphi_s}{\varphi_t}\left(\left(\frac{p_s}{p^\star}\right)^{1+\alpha} - 1\right)\right) \tag{C6}$$

The average longwave cooling is then obtained by dividing by the layer depth $\Delta p = p_s - p^\star$ in equation (14).

Open Research Section

The codes developed for radiative transfer calculations with and without moist intrusions can be found here: `https://zenodo.org/badge/latestdoi/523001540` and the scripts developed for all data analysis can be found here: `https://doi.org/10.5281/zenodo.7401107`.

Acknowledgments

The authors gratefully acknowledge diverse funding agencies and resources used for this work. B.F. and C.M. thank funding from the European Research Council (ERC) under the European Union's Horizon 2020 research and innovation program (Project CLUSTER, grant agreement No 805041), and the EUREC^{4}A campaign organizers for giving the opportunity to take part to the campaign and use the data early on. R. P. was supported by the US National Science Foundation (award AGS 19-16908), by the National Oceanic and Atmospheric Administration (award NA200AR4310375), and the Vetlesen Foundation. .

References

Albright, A. L., Fildier, B., Touzé-Peiffer, L., Pincus, R., Vial, J., & Muller, C. (2021, feb). Atmospheric radiative profiles during EUREC4A. *Earth System Science Data Discussions*, *13*(2), 617–630. Retrieved from `https://essd.copernicus.org/articles/13/617/2021/` doi: 10.5194/essd-13-617-2021

Bony, S., Schulz, H., Vial, J., & Stevens, B. (2020, jan). Sugar, Gravel, Fish, and Flowers: Dependence of Mesoscale Patterns of Trade-Wind Clouds on Environmental Conditions. *Geophysical Research Letters*, *47*(7). doi: 10.1029/2019gl085988

Bretherton, C. S., & Blossey, P. N. (2017, dec). Understanding Mesoscale Aggregation of Shallow Cumulus Convection Using Large-Eddy Simulation. *Journal of Advances in Modeling Earth Systems*, *9*(8), 2798–2821. Retrieved from `https://onlinelibrary.wiley.com/doi/abs/10.1002/2017MS000981` doi: 10.1002/2017MS000981

Bretherton, C. S., Blossey, P. N., Khairoutdinov, M., Bretherton, C. S., Blossey, P. N., & Khairoutdinov, M. (2005, dec). An Energy-Balance Analysis of Deep Convective Self-Aggregation above Uniform SST. *Journal of the Atmospheric Sciences*, *62*(12), 4273–4292. Retrieved from http://journals.ametsoc.org/doi/abs/10.1175/JAS3614.1 doi: 10.1175/JAS3614.1

Craig, G. C., & Mack, J. M. (2013, aug). A coarsening model for self-organization of tropical convection. *Journal of Geophysical Research Atmospheres*, *118*(16), 8761–8769. doi: 10.1002/jgrd.50674

George, G., Stevens, B., Bony, S., Pincus, R., Fairall, C., Schulz, H., ... Radtke, J. (2021). Joanne: Joint dropsonde observations of the atmosphere in tropical north atlantic meso-scale environments. *Earth System Science Data*, *13*(11), 5253–5272. doi: 10.5194/essd-13-5253-2021

Hogan, R. J., & Matricardi, M. (2020, dec). Evaluating and improving the treatment of gases in radiation schemes: The Correlated K-Distribution Model Intercomparison Project (CKDMIP). *Geoscientific Model Development*, *13*(12), 6501–6521. doi: 10.5194/GMD-13-6501-2020

Holloway, C. E., Wing, A. A., Bony, S., Muller, C., Masunaga, H., L'Ecuyer, T. S., ... Zuidema, P. (2017). Observing Convective Aggregation. *Surveys in Geophysics*, *38*(6), 1199–1236. Retrieved from https://doi.org/10.1007/s10712-017-9419-1 doi: 10.1007/s10712-017-9419-1

Jeevanjee, N., & Fueglistaler, S. (2020a, feb). On the cooling-to-space approximation. *Journal of the Atmospheric Sciences*, *77*(2), 465–478. Retrieved from www.ametsoc.org/PUBSReuseLicenses doi: 10.1175/JAS-D-18-0352.1

Jeevanjee, N., & Fueglistaler, S. (2020b). Simple spectral models for atmospheric radiative cooling. *Journal of the Atmospheric Sciences*, *77*(2), 479–497. doi: 10.1175/JAS-D-18-0347.1

Kluft, L., Dacie, S., Brath, M., Buehler, S. A., & Stevens, B. (2021). Temperature-Dependence of the Clear-Sky Feedback in Radiative-Convective Equilibrium. *Geophysical Research Letters*, *48*(22), 1–10. doi: 10.1029/2021GL094649

Krebs, G. D. (2022). *Harmony A, B (Earth Explorer 10).* Retrieved November 29, 2022, from https://space.skyrocket.de/doc_sdat/harmony.htm

Lerner, J. A., Weisz, E., & Kirchengast, G. (2002). Temperature and humidity retrieval from simulated Infrared Atmospheric Sounding Interferometer (IASI) measurements. *Journal of Geophysical Research Atmospheres*, *107*(14), 1–11.

Muller, C., & Bony, S. (2015, jul). What favors convective aggregation and why? *Geophysical Research Letters*, *42*(13), 5626–5634. doi: 10.1002/2015GL064260

Muller, C., Yang, D., Craig, G., Cronin, T., Fildier, B., Haerter, J. O., ... Sherwood, S. C. (2022, jan). Spontaneous Aggregation of Convective Storms. *https://doi.org/10.1146/annurev-fluid-022421-011319*, *54*(1), 133–157. Retrieved from https://www.annualreviews.org/doi/abs/10.1146/annurev-fluid-022421-011319 doi: 10.1146/ANNUREV-FLUID-022421-011319

Muller, C. J., & Held, I. M. (2012, aug). Detailed Investigation of the Self-Aggregation of Convection in Cloud-Resolving Simulations. *Journal of the Atmospheric Sciences*, *69*(8), 2551–2565. Retrieved from http://journals.ametsoc.org/doi/abs/10.1175/JAS-D-11-0257.1 doi: 10.1175/JAS-D-11-0257.1

Muller, C. J., & Romps, D. M. (2018, mar). Acceleration of tropical cyclogenesis by self-aggregation feedbacks. *Proceedings of the National Academy of Sciences*, *115*(12), 2930–2935. Retrieved from http://www.ncbi.nlm.nih.gov/pubmed/29507192http://www.pubmedcentral.nih.gov/articlerender.fcgi?artid=PMC5866587http://www.pnas.org/lookup/doi/10.1073/pnas.1719967115 doi: 10.1073/pnas.1719967115

Narenpitak, P., Kazil, J., Yamaguchi, T., Quinn, P., & Feingold, G. (2021, oct). From Sugar to Flowers: A Transition of Shallow Cumulus Organization Dur-

ing ATOMIC. *Journal of Advances in Modeling Earth Systems*, *13*(10), e2021MS002619. Retrieved from https://onlinelibrary.wiley.com/doi/full/10.1029/2021MS002619https://onlinelibrary.wiley.com/doi/abs/10.1029/2021MS002619https://agupubs.onlinelibrary.wiley.com/doi/10.1029/2021MS002619 doi: 10.1029/2021MS002619

Pierrehumbert, R. T. (1994). Thermostats, Radiator Fins, and the Local Runaway Greenhouse. *Journal of the Atmospheric Sciences*, *52*(10), 1784–1806. doi: 10.1175/1520-0469(1995)052⟨1784:TRFATL⟩2.0.CO;2

Pierrehumbert, R. T. (2012, jun). Radiative transfer in temperature-stratified atmospheres. In *Principles of planetary climate* (pp. 187–315). Cambridge University Press. doi: 10.1017/CBO9780511780783.006

Pincus, R., Mlawer, E. J., & Delamere, J. S. (2019, oct). Balancing Accuracy, Efficiency, and Flexibility in Radiation Calculations for Dynamical Models. *Journal of Advances in Modeling Earth Systems*, *11*(10), 3074–3089. Retrieved from https://onlinelibrary.wiley.com/doi/abs/10.1029/2019MS001621 doi: 10.1029/2019MS001621

Prange, M., Brath, M., & Buehler, S. A. (2021). Are elevated moist layers a blind spot for hyperspectral infrared sounders? A model study. *Atmospheric Measurement Techniques*, *14*(11), 7025–7044. doi: 10.5194/amt-14-7025-2021

Prange, M., Buehler, S. A., & Brath, M. (2022). How adequately are elevated moist layers represented in reanalysis and satellite observations ? *EGUsphere*(August), 1–26.

Romps, D. M. (2014). An analytical model for tropical relative humidity. *Journal of Climate*, *27*, 7432–7449. doi: 10.1175/JCLI-D-14-00255.1

Ruppert, J. H., & Hohenegger, C. (2018, jun). Diurnal Circulation Adjustment and Organized Deep Convection. *Journal of Climate*, *31*(12), 4899–4916. doi: 10.1175/JCLI-D-17-0693.1

Schulz, H. (2022). C^{3}ontext: a common consensus on convective organization during the eurec^{4}a experiment. *Earth System Science Data*, *14*(3), 1233–1256. doi: 10.5194/essd-14-1233-2022

Schulz, H., Eastman, R., & Stevens, B. (2021). Characterization and Evolution of Organized Shallow Convection in the Downstream North Atlantic Trades. *Journal of Geophysical Research: Atmospheres*, *126*(17), 1–18. doi: 10.1029/2021JD034575

Schulz, H., & Stevens, B. (2018, oct). Observing the Tropical Atmosphere in Moisture Space. *Journal of the Atmospheric Sciences*, *75*(10), 3313–3330. Retrieved from http://journals.ametsoc.org/doi/10.1175/JAS-D-17-0375.1 doi: 10.1175/JAS-D-17-0375.1

Seeley, J. T., & Jeevanjee, N. (2021). H2O Windows and CO2 Radiator Fins: A Clear-Sky Explanation for the Peak in Equilibrium Climate Sensitivity. *Geophysical Research Letters*, *48*(4), 1–12. doi: 10.1029/2020GL089609

Shamekh, S., Muller, C., Duvel, J. P., & D'Andrea, F. (2020, nov). Self-Aggregation of Convective Clouds With Interactive Sea Surface Temperature. *Journal of Advances in Modeling Earth Systems*, *12*(11), e2020MS002164. Retrieved from https://onlinelibrary.wiley.com/doi/full/10.1029/2020MS002164https://onlinelibrary.wiley.com/doi/abs/10.1029/2020MS002164https://agupubs.onlinelibrary.wiley.com/doi/10.1029/2020MS002164 doi: 10.1029/2020MS002164

Singh, M. S., & O'Gorman, P. A. (2012). Upward shift of the atmospheric general circulation under global warming: Theory and simulations. *Journal of Climate*, *25*(23), 8259–8276. doi: 10.1175/JCLI-D-11-00699.1

Sokol, A. B., & Hartmann, D. L. (2022, jul). Congestus mode invigoration by convective aggregation in simulations of radiative-convective equilibrium. *Journal of Advances in Modeling Earth Systems*, *14*(7). doi: 10.1029/2022ms003045

Stevens, B., Bony, S., Brogniez, H., Hentgen, L., Hohenegger, C., Kiemle, C., ...

Zuidema, P. (2020, jan). Sugar, gravel, fish and flowers: Mesoscale cloud patterns in the trade winds. *Quarterly Journal of the Royal Meteorological Society*, *146*(726), 141–152. Retrieved from https://onlinelibrary.wiley.com/doi/abs/10.1002/qj.3662 doi: 10.1002/qj.3662

Stevens, B., Bony, S., Farrell, D., Ament, F., Blyth, A., Fairall, C., ... Zöger, M. (2021, aug). EUREC4A. *Earth System Science Data*, *13*(8), 4067–4119. doi: 10.5194/ESSD-13-4067-2021

Stevens, B., Brogniez, H., Kiemle, C., Lacour, J. L., Crevoisier, C., & Kiliani, J. (2017, nov). *Structure and Dynamical Influence of Water Vapor in the Lower Tropical Troposphere* (Vol. 38) (No. 6). Springer Netherlands. Retrieved from http://link.springer.com/10.1007/s10712-017-9420-8 doi: 10.1007/s10712-017-9420-8

Wei, P. S., Chiu, H. H., Hsieh, Y. C., Yen, D. L., Lee, C., Tsai, Y. C., & Ting, T. C. (2019, jan). Absorption coefficient of water vapor across atmospheric troposphere layer. *Heliyon*, *5*(1), e01145. doi: 10.1016/J.HELIYON.2019.E01145

Wing, A. A., Emanuel, K., Holloway, C. E., & Muller, C. (2017, nov). Convective Self-Aggregation in Numerical Simulations: A Review. *Surveys in Geophysics*, *38*(6), 1173–1197. Retrieved from http://link.springer.com/10.1007/s10712-017-9408-4 doi: 10.1007/s10712-017-9408-4